LASER-INDUCED GRAPHENE ELECTRODES FOR ORGANIC ELECTROCHEMICAL TRANSISTORS (OECTS)

MOHAMMAD NAZERI

A THESIS SUBMITTED TO
THE FACULTY OF GRADUATE STUDIES
IN PARTIAL FULFILLMENT OF THE REQUIREMENTS
FOR THE DEGREE OF
MASTER OF APPLIED SCIENCE

GRADUATE PROGRAMME IN ELECTRICAL ENGINEERING
AND COMPUTER SCIENCE
YORK UNIVERSITY
TORONTO, ONTARIO

DECEMBER 2022

ABSTRACT

Organic electrochemical transistors (OECTs) have drawn a lot of interest because of their low cost, biocompatibility, and ease of fabrication, allowing them to be utilized in various applications including flexible displays, electrochemical sensing, and biosensing. Key components of OECTs are the gate, source, and drain electrodes. Here, OECTs with laser-induced graphene (LIG) electrodes are presented. The electrode patterns for the source, drain, and gate are created by lasing the polymer substrate polyimide (PI). The entire process is simple and inexpensive without complicated chemical synthesis routines or expensive materials such as gold. Patterns can be customized quickly and digitally. Different laser parameters play an important role in changing the conductivity and porosity of the graphene leading to its use in different applications. The low-cost and porous LIG electrodes with low contact resistance, good electrical stability, and adhesion to the polymeric substrate play an essential role in device performance. Due to the flexibility of the laser process, source, drain, and gate can potentially have different properties even though they are fabricated together in a co-planar architecture. The minimum sheet resistance achieved with this laser method for the square patterned electrodes is 7.86 Ω/sq. The LIG-based OECTs demonstrate good electrical modulation and high on-current. The LIG-based OECT shows low OFF current in the order of 0.035 mA.

ACKNOWLEDGEMENTS

I would like to acknowledge and give my warmest thanks to my supervisor Dr. Gerd Grau who made this work possible. His guidance and advice carried me through all the stages of my projects. He has the attitude and the substance of a genius, who continually and convincingly conveyed a spirit of adventure regarding research. I have learned to become a researcher due to his guidance and persistent help. I also would like to thank Dr. Paul O'Brien, who consented to serve on my supervisory committee and who has offered to assist me whenever I have had difficulties. I'm grateful that Dr. Reza Rizvi graciously agreed to take part in my oral examination.

I wish to express my gratitude to Veronica Di Cecco at the Royal Ontario Museum and Magdalena Jaklewicz at York University's Advanced Light and Electron Microscopy Facility for their prompt characterization assistance whenever I needed it. I acknowledge the support of the Natural Sciences and Engineering Research Council of Canada (NSERC).

I would like to thank all my lab mates, specially Milad and Mohamad, who always supported me mentally and made the lab work more pleasurable. I also like to thank Benno, who worked with me for a period of time.

I am most grateful to my dear family for supporting me in all stages of my life and making me progress always even from a long distance. I would specially thank to my parents for always trying to give me the best and encouraging me in every single moment of my life.

TABLE OF CONTENTS

LIST OF TABLES

LIST OF FIGURES

Chapter 1 . INTRODUCTION

1.1. Graphene

Nowadays, due to its extraordinary properties the use of carbon in various structures has been rapidly expanding in recent years. The layers formed form 3D graphite structures and are kept together by van der Waals forces. [1]. Carbon has a large number of allotropes including fullerene (0D) [2], carbon nanotubes (CNTs) [3], diamond, graphite, amorphous carbon, and graphene sheet which are shown in Figure **1-1**. Demonstration of various forms of carbon nanostructures [4].

In other words, graphene is a single layer of carbon atoms in a two-dimensional (2D) structure that has sp^2 hybridised C-C bonds with π-electron clouds [5]. The three primary forms of graphene are single layer, few layers (5–10 layers are typical), and multilayer graphene, which is 20–30 layers thick. [6]. Graphene's properties could change based on the number of layers. One of the key differences between single-layer and multilayer graphene is the band gap. The single-layer graphene has a zero bandgap; however, the electrical structure and the bandgap of multilayer graphene can be altered. Therefore, multilayer graphene can be used in many different applications, including optoelectronics. [7]. As the number of layers increases, surrounding layers constrain each layer in a multilayer construction. This restriction and its interactions with other layers reduce phonon transport. Therefore,

compared to single-layer graphene, multilayer graphene will have lower heat conductivity [8]. It shows a higher carrier mobility ($\mu > 10^4$ cm^2/Vs) compared to the other metal electrodes which are in the range of 10-50 cm^2/Vs [9].

Due to the conduction band and valance band of this material overlapping at two places in the Brillouin zone, it has a very large carrier mobility at room temperature [10].

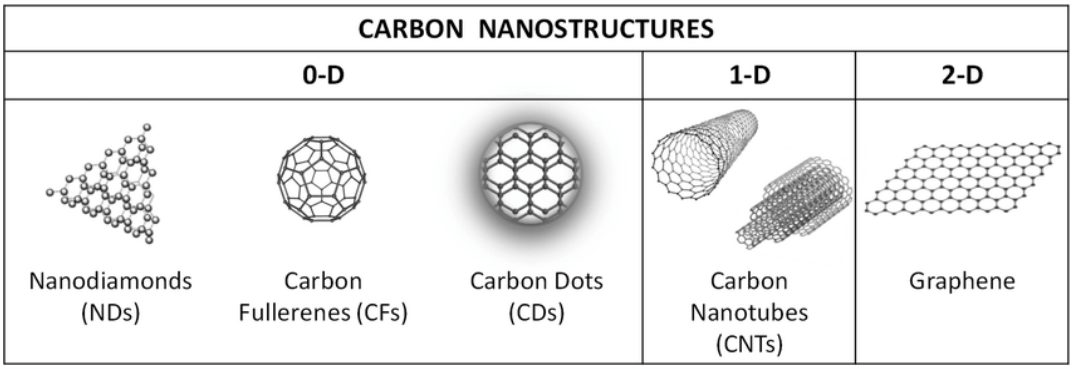

Figure 1-1. Demonstration of various forms of carbon nanostructures. Figure is reproduced with permission from Ref. [4].

Graphene has outstanding mechanical qualities. Graphene is perfect for a variety of applications due to its great strength, rigidity, and toughness. Graphene's hexagonal lattice can tolerate deformations thanks to its sp^2 bonding. With an intrinsic strength of 130 GPa, the defect-free layer of graphene is regarded as the strongest material ever discovered. Additionally, it may be stretched 20% beyond its original length [11].

In recent years, graphene has been introduced as an important material for some applications such as batteries, transistors, and biosensors [12]. It has attracted attention due to the high charge carrier mobility ($\mu > 10^4$ cm^2/Vs) [9], optical transparency (2.3% absorption) [6], excellent electrical conductivity [13], superior thermal conductivity (up to 5.3×10^3 $W.m^{-1}.K^{-1}$) [14], high surface area (2600 m^2/g) [15], and remarkable stiffness [16]. Due to the unique properties mentioned above, graphene has been an emerging material for industrial fields like electronics, healthcare, and energy. Hence, investigating and optimizing the various synthesis methods of graphene play an essential role in commercializing this material [17].

1.2. Graphene Fabrication

Graphene can be synthesised using a variety of ways; however, they can be categorised into top-down and bottom-up strategies.

Graphene sheets are produced in the top-down method through the separation of graphite or graphite oxide. Graphite powder is typically reduced or exfoliated using this technique. One must overcome the van der Walls forces holding the layers of graphite together in order to separate them and produce graphene. The process of separation could be challenging despite the deterioration of these bonding forces. The most popular top-down procedures are chemical oxidation-reduction, electrochemical exfoliation, and mechanical exfoliation. [18].

In contrast to top-down techniques, bottom-up strategies create graphene sheets using carbon gases. In other words, the bottom-up method is a type of nanomaterial synthesis process that is based on the self-assembly of building blocks. These techniques, which are frequently chemical in origin, allow manipulation of the nanoscale structure. High temperatures are necessary for high material quality and high levels of graphitization. The most popular bottom-up techniques include pyrolysis, epitaxial growth, and chemical vapour deposition (CVD). When compared to the top-down approach, outstanding controllability over graphene's morphology and graphene surfaces with fewer defects may be achieved.Graphene nanoribbons and graphene flakes are typically good candidates for the bottom-up approaches, while graphene sheets with a large surface area are not since the layer becomes wrinkled; the substrate becomes contaminated, resulting in unintended doping of the pure graphene; and there is difficulty in separating the huge sheets of graphene from the CVD substrate and rolling them off to the appropriate substrate [19].

One of the most used techniques for synthesising graphene, exfoliation, was developed as the opposite of stacking. In general, the weak van der Waals forces between the layers of graphene within the graphite structure must be overcome by the longitudinal or transverse stress in order for mechanical exfoliation to occur. [20]. According to some reports, graphene could be created using a variety of

mechanical exfoliation techniques like sonication and micromechanical cleavage. [21]. It is not practicable for mass manufacturing because of the uneven thickness of the produced films and the high cost caused by the low yield in this technique. Although single-layer and multilayer graphene can be produced through mechanical exfoliation, the resulting single layer typically has a very small surface area [22].

The most effective way to create high-quality graphene with a substantial surface area is using CVD. As one of the bottom-up techniques, CVD is described as depositing a stable solid layer on a substrate by chemical reactions sparked by the activation gas reagents and high temperature. In other words, activated carbon sources breakdown in a plasma environment or at high temperatures and then are deposited on the substrate of interest. [23]. The development process can be influenced by various factors such as temperature, gas flow, and pressure. Also, using this technique, graphene doping is achievable. The CVD technique can be used to create graphene in both single-layer and multilayer forms [24].

Despite being scalable, CVD procedures are not cost-effective, and their by-products are frequently hazardous. The CVD method's most difficult problem is getting the graphene onto the target substrate. Three steps essentially sum up this transfer. To prevent cracking during the transfer, a layer of transfer media is first necessary. [25]. When utilized as a supporting layer, polymers like polymethyl methacrylate (PMMA) aid in the homogeneity of the generated graphene sheet. In

order to transfer the graphene sheet onto the target substrate, the graphene sheet must first be cut free from the growth substrate. For this operation, using different etchants or exposing the substrate to oxygen is advised. Last but not least, the oxygen plasma treatment's provision of a strong contact between the generated graphene sheet and the substrate is absolutely vital. [26].

Printing is another viable method of depositing graphene. For various uses, diverse designs can be placed on large-scale flexible substrates. Although printed electronics' first applications were in displays and lighting, they are now showing promise in a variety of sectors, including automotive and transportation, consumer electronics, healthcare, packaging, aerospace, and architecture [27]. Printed electronics methods include extrusion printing, screen printing, gravure printing, and ink-jet printing. By adjusting the process parameters in these approaches, it is simple to control the graphene's thickness. It has been reported in several studies that printed graphene electrodes can be used in wearable and flexible electronics [28][29]. Although high-resolution graphene patterns can be produced using inkjet, transfer, and gravure printing techniques, screen-printing is a practical choice when low resistance is needed because it can create thick films in a single pass, which shortens processing times. The challenge of completely eliminating the binder or surfactant elements of the inks from the printed patterns is one of the disadvantages. While improving the stability and printability of graphene inks, the binder or

surfactant also coats the graphene flakes in a substance with limited conductivity [30]. Recently, a simple method using laser processing has been introduced to eliminate the mentioned disadvantages of the fabrication methods.

1.3. Laser-Induced Graphene

By using a CO_2 laser, the polymeric substrate can be converted to LIG in the simplest possible way shown in Figure 1-2.

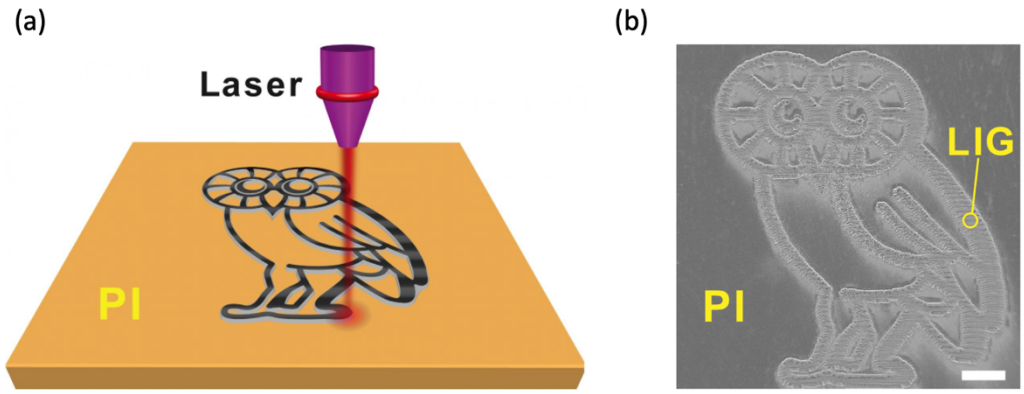

Figure 1-2. (a) Laser process on PI substrate. (b) Flexible LIG pattern on PI substrate. Figure is reproduced with permission from [31].

Despite the fact that a conducting carbon network was initially created in 1994 using an ultraviolet (UV) laser [32], Lin et al. [31] were the first researchers to show LIG synthesis using a CO_2 laser in 2014. It is reported that LIG can be generated on polyimide (PI), polyetherimide (PEI), polyether ether ketone (PEEK), and other high-temperature polymers using a CO_2 laser. LIG was discovered to be produced

by a variety of substrates, including wood, potatoes, and papers. This demonstrates that LIG may be applied to a variety of surfaces with improved conductivity and a sheet resistance of only 5 Ω/sq as shown in Figure 1-3 [33].

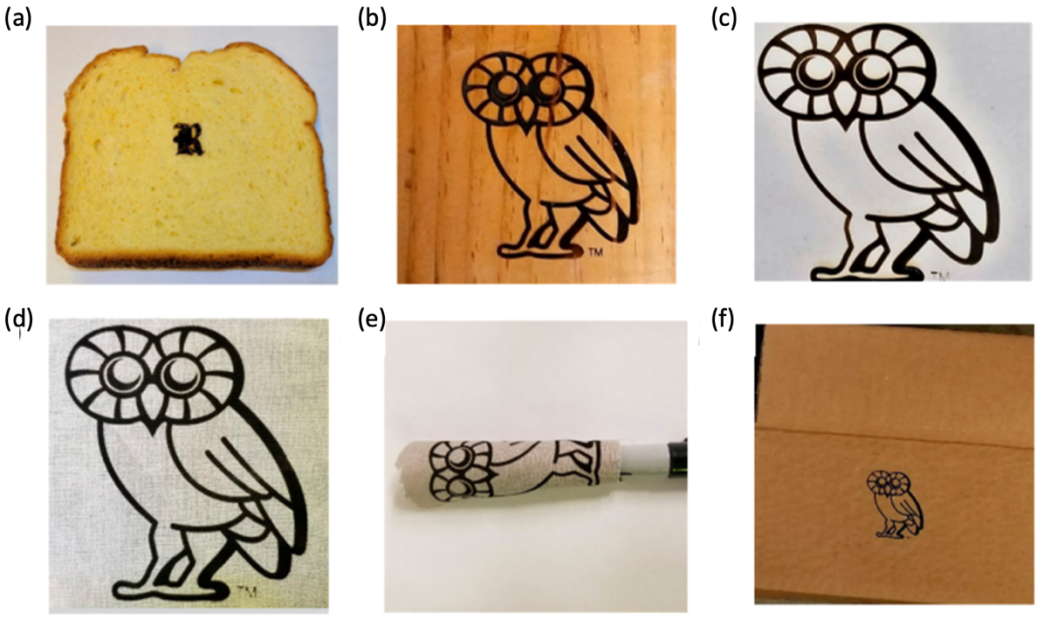

Figure 1-3. LIG made on a) bread, b) pinewood, c) cotton paper, d) muslin cloth, e) cloth, f) cardboard. Figure is reproduced with permission from [33].

The conversion of the polymer into LIG may be influenced by the aromatic segments in the polymer structures. Rapid temperature rises cause C-O and C-N bonds to thermally decompose. After this decomposition, the rearrangement occurs creating the aromatic segments which increases the chance of the LIG forming [34].

The type of substrate used to create LIG has a big impact on how it behaves. This is due to the fact that the phenolic structures found in the precursor substrates contain

a variety of functional groups attached to them that, if not eliminated during the lasing process, display different behaviours and change the characteristics of LIG when they interact with other external molecules. It is quite difficult to eliminate these extra functional groups that affect LIG's characteristics. Given that the majority of the raw materials used to make LIG are largely carbonaceous and contain generally hydrocarbons or polymers, the functional LIG that is produced mainly consists of oxidized species that act as impurities in the otherwise pure LIG [35][36].

Although the majority of reports demonstrate the single scribing method for producing LIG [31][37], there are few reports that show the importance of the multiple passes and maximizing the energy delivery to the substrate by using the defocusing concept. [33][38]. In fact, these multiple passes can be helpful in the conversion of some other substrates such as epoxy and phenolic resin to LIG. This process is divided into two sections: the first part during which the polymeric substrate is converted to the amorphous graphene known as an “intermediate phase”. The second lasering leads to the LIG fabrication from the intermediate phase. Regarding the focusing concept, different levels of focus could be attained simply by adjusting the distance between the laser and the substrate used for LIG manufacturing due to the laser focus having the shape of a hyperbolic cone [33].

Scanning the laser beam can easily pattern graphene without requiring complex chemical synthesis procedures. Laser patterning of graphene has two significant advantages: it allows for the laser patterning of LIG on a range of substrates, allowing for greater flexibility in the materials used to make LIG. Second, it can be used in roll-to-roll processes, allowing for large-scale, mass production of LIG that might be used a conductor in supercapacitors [39][40], electrochemical sensors [41], batteries [42][43], and in antibacterial applications [44].

1.4. LIG Applications

Due to the development of portable and wearable electronics, miniature energy storage devices are now required. Because they offer quicker charge-and-discharge cycles and greater long-term endurance than microbatteries, microsupercapacitors (MSCs) are preferable to microbatteries [45]. A MSC on a sheet of PI was demonstrated using the initial work on LIG. Even at a high voltage scan rate of 10,000 mV/s^1, the pseudo-rectangular shape was maintained, and the specific areal capacitance (CA) was maintained over 1 mF/cm^2, which indicates the applicability of the device in high power electronic applications. This LIG-MSC performed better than other carbon-based MSCs due to its high capacitance, which ranges from 1.3 to 3.9 mF cm^{-2} [46]. Another work demonstrated that LIG electrodes were used in microsupercapacitors, leading to enhanced capacitance [31]. It is reported that the

LIG-MSC has 100 times larger specific areal energy than reduced graphene oxide based MSC. Also, LIG-MSC demonstrates four times larger power density [31].

In another work, it was shown that LIG fabricated on polyimide substrate can subsequently be used to construct flexible, stacking supercapacitors with improved capacitive performance illustrated in Figure 1-5 (d). Devices employing solid-state polymeric electrolytes (PVA/H_2SO_4) show areal capacitance of more than 9 mF/ cm^2 at a current density of 0.02 mA/cm^2, which is more than twice that of traditional aqueous electrolytes [47].

In addition to the MSC application, LIG electrodes have been widely used in sensing applications. LIG electrodes have been widely used in mechanical sensors due to the excellent mechanical performance and high conductivity. In one report, the wavy-LIG strain sensor was fabricated by using a wavy plastic mold as a substrate. The 3D wavy LIG was created by scanning PI film with a laser on a mold's wavy surface. The wavy-LIG strain sensor was created when LIG was placed on a silicone rubber substrate and packaging operation was complete. When the sensor was stretched, the wavy construction caused the stress to concentrate on the troughs, which led to a significant shift in resistance. Stretching revealed ordered spaced stripes and fewer holes in the wavy-LIG strain sensor shown in Figure **1-4**, demonstrating the capacity to prevent LIG degradation and enable reversible recovery. The low hysteresis and high sensitivity of GF = 37.8 was achieved which

shows its ability to be used for detecting the muscle and joint movement as a wearable flexible strain sensor [48].

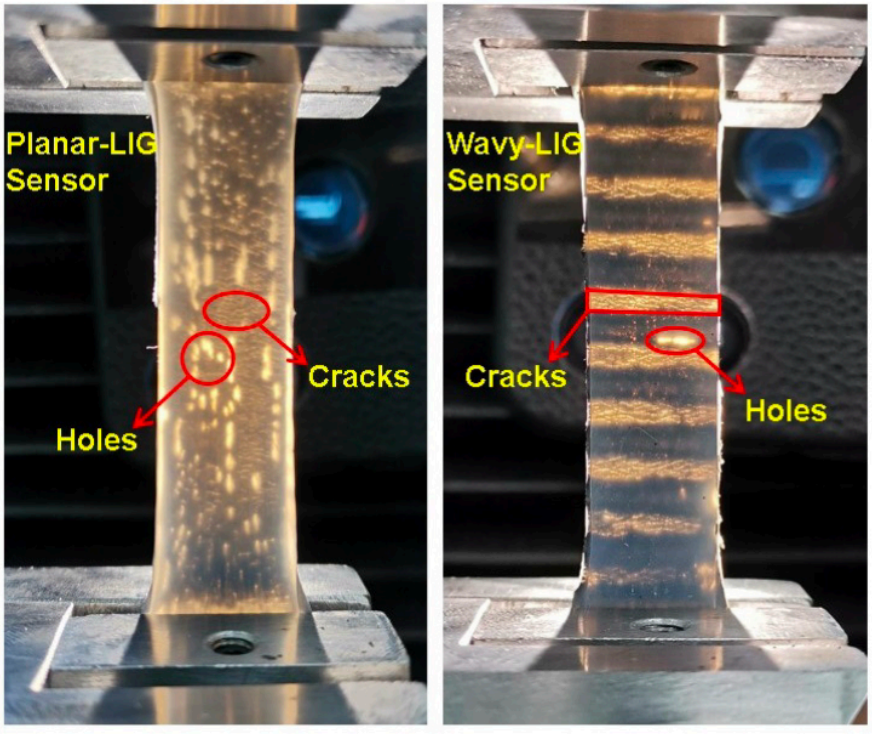

Figure 1-4. The tensile testing of wavy-LIG and planar-LIG sensors. Figure is reproduced with permission from [48].

Since the initial realisation of the LIG-based capacitor in 2014 [31], better precursor materials and structural designs have been investigated to create LIG-based devices with controllable morphologies and customised characteristics.

Tao et al. [49] demonstrate that LIG is an excellent material for thermal sound sources due to its strong thermal conductivity and low heat capacity. Additionally,

the LIG porous structure makes it appropriate for sound detection because it is sensitive to low vibration. The LIG artificial throat shown in Figure 1-5 (a) can generate wideband sound with frequencies ranging from 100 Hz to 40 kHz when used as a sound source. Sound can likewise be produced by the artificial throat. The device produces sound waves when an alternating voltage is applied because the periodic heat expands the air. The device can thus function as a sound source and detector at the same time [49].

Systems that can record physical and kinematic data like temperature, heart rate, and ECG in real time have made advancements in the field of wearable physical sensing platforms. Human sweat contains a wealth of health-related data and may enable non-invasive molecular monitoring. Therefore, a flexible five-electrode graphene sensor patch made with lasering on a polyimide (PI) substrate is shown in Figure 1-5 (b). It is reported that vital information for response to the stress may be retrieved from cortisol secreted in sweat using flexible five-electrode graphene-based wireless sensing device [50].

Singh et al. [51] show the powerful antibacterial activity of LIG's nanofibrous texture and sharp edges is further boosted by the addition of metal and metal oxides. Due to its high conductivity, it exhibits fascinating Joule heating abilities as well as applications for self-sterilization in both air and water. Additionally intended for use against the coronaviruses HCoV-OC43 and HCoV-229E shown in Figure 1-5

(c), this resulted in the total eradication of the virus within 15 minutes of photothermal action. Due to its low oxygen overpotential, it also has good electrochemical characteristics. Hydrogen peroxide puts the bacteria under oxidative stress and kills them. [51].

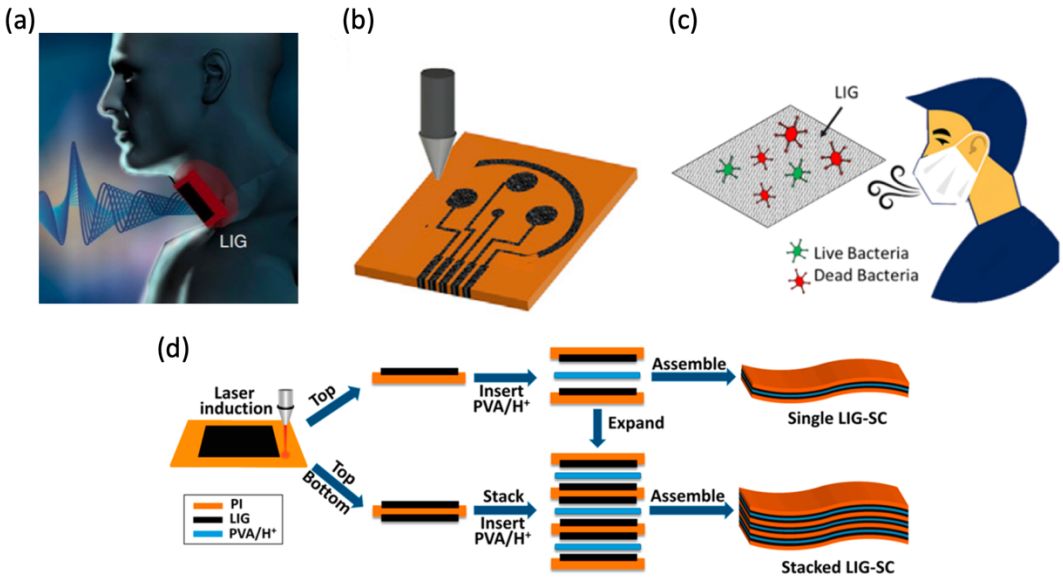

Figure 1-5. a) Artificial throat made via LIG function as a sound source and detector. Figure is reproduced with permission from [49]. (b) A flexible five-electrode LIG sensor for cortisol investigation in sweat. Figure is reproduced with permission from [50]. (c) LIG's nanofibrous texture helpful in killing bacteria against the coronaviruses HCoV-OC43 and HCoV-229E. Figure is reproduced with permission from [51]. (d) A schematic depiction of the fabrication process for stacking LIG supercapacitors. Figure is reproduced with permission from [47].

Although LIG electrical conductivity paired with its great flexibility made it possible to use in some electronic devices such as sensors, supercapacitors, and wearable technology, there has not been any reports in transistors yet.

1.5. Organic Electrochemical Transistors (OECTs)

The semiconductor devices known as transistors serve as switches or amplifiers in electrical circuits. Transistors typically have at least three terminals: source, drain, and gate. The current through another pair of terminals can be changed by providing current or voltage to the third terminal. Integrated circuits frequently contain transistors, however some of them may also be used separately. Organic electrochemical transistors (OECTs), a type of organic transistor, have been widely used in applications such as monitoring cells and ion sensing. Key parts include a gold or metallic source and drain contact, conducting polymer channel that is in contact with an electrolyte, in which the gate electrode is immersed. The electrodes can be designed in different ways. A typical OECT structure is shown in Figure 1-6 [52].

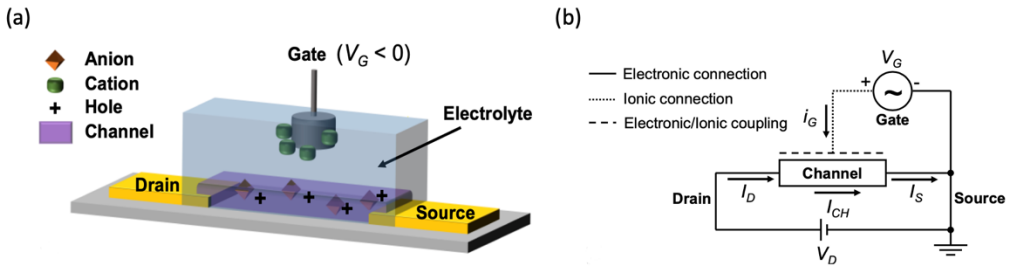

Figure 1-6. (a) OECT device structure. (b) Electrical connection in OECT. Figure is reproduced with permission from [52].

As shown in Figure 1-6, OECT performance depends on two different circuits; one would be ionic that has gate electrode and electrolyte in the channel and the other one is called electronic where source and drain and semiconductor exist. According to the Bernards model [53]., electrochemical capacitor is modeled to explain the ionic circuit, while concepts from solid-state physic explains the electronic system. When the positive gate voltage is applied, anions shift to the top plate and cations shift to the bottom one. Although the compensation occurs in the bulk, there are excess ions close to the interfaces. Two voltage drops are considered in the interfaces called electrochemical double layers. Two capacitors are modeled in the interfaces with an electrolyte that plays a role as a resistor [53].

Organic semiconductor materials are widely used as channel material for OECTs. They address some of the drawbacks of silicon. Silicon cannot be in contact with electrolyte. Oxide or nitrite can be created for protecting the silicon from corrosion,

but ions from electrolyte will not be able to penetrate in silicon. Ions must go into the semiconductor and couple volumetrically with electronic charges. Some polymers have hydrophobic side chain which does not let the ions come inside the channel. Also, some polymers are very dense, and ions cannot physically penetrate [54].

A typical doped semiconductor, PEDOT:PSS, consist of two main chains. One is conjugated polythiophene chain in which dioxy bridge exists to make it a little bit more hydrophilic and more electrochemically stable. Another chain called polystyrene sulfonate has sulfonate anions compensated with either protons or sodium cations. Some of those are uncompensated and are electrically compensated by a hole on the polythiophene chain [55]. The doping and de-doping does not happen instantaneously [56]. Inkjet printing is the common method for fabrication of organic semiconductor material as a semiconductor channel in transistors. This method can directly pattern different functional materials on a substrate. The details of inkjet printing are discussed in section 1.6.

Selecting the electrode materials is an important step in fabricating OECT. The electrodes should be resistant against corrosion, highly conductive, biocompatible, and low cost. For the gate electrode, the material should have high capacitance to make the voltage drop at the interface of electrolyte and semiconductor channel small leading to the more efficient transistor [57]. In OECT devices, several

materials and methods have been widely used for fabricating the electrodes. A promising material, indium tin oxide (ITO) has a high optical transmittance and good conductivity. However, there are some drawbacks like the price of indium, its difficulty to be printed on flexible substrates, and its brittleness which leads to a sharp decrease in the electrical conductivity with bending [58]. The noble metals like gold [59], palladium [60], and platinum [61] have long been considered among the best metals for source and drain electrodes in OECTs. Han and coworkers [62] created OECTs on narrow probes used as amplifying transducers of biological signal. Gold was used as electrode material and Ti adhesion layer as interconnects using e-beam evaporation. It is demonstrated that, local gate configuration is necessary for biological application since the local gating can monitor the local changes of materials such as glucose by the help of biorecognition elements attached to the gate electrode. Biological application needs the small local gating. With a high resistive interconnect, a low transconductance and a high threshold voltage are reported. Since the dimension of the local gate electrode cannot be increased, something should happen to increase the capacitance between the gate electrode and electrolyte, which helps most of the applied V_g to be dropped at the OECT channel. Using mixed ionic/electronic conductive material such as PEDOT:PSS doped with perchlorate (ClO_4) as a coating on top of the small local gate is helpful for increasing the OECT transconductance [62]. In one report, gold nanowires have been used as electrodes in stretchable organic transistors. These electrodes can be

used to obtain high-performance transistors due to the well-matched work function. Strain sensitivity is a problem of these gold nanowires electrodes [63]. A major drawback of these noble metals is their high cost.

In general, not only some of these materials themselves have disadvantages such as price to be used as electrodes, but there are also difficulties with fabricating them. Traditional methods to fabricate electrodes, such as metal evaporation and lithography, are costly, slow, and cannot be customized easily. In particular, photolithography can lead to problems in the fabrication of electrodes on organic semiconductor films since the films can be damaged by the photoresist [64]. Although Makita et al. transferred metal electrodes to another substrate to prevent the damage from photoresist, there are still several challenges, such as the use of high vacuum and thermal damage during the vacuum evaporation [64]. Printed electrodes can overcome some of these limitations; however, this typically still requires multiple steps, synthesis of nanomaterials, and formulation of inks containing nanomaterials, which can be costly [65].

To overcome these challenges, graphene-based materials can be an alternative to ITO and evaporated metals due to their advantageous properties, especially their high surface area [66]. For fabricating graphene-based electrodes, some common methods include chemical vapor deposition (CVD), molecular beam epitaxy

(MBE), and chemical synthesis; however, there are still some challenges in terms of the cost and difficulties during the fabrication process [23].

To further investigate methods for fabricating graphene-based electrodes, there is frequently a larger demand for quick design changes and digitally enabled direct-write procedures in low-volume, late-stage manufacturing. Malliaras and coworkers [67] reported the source and drain electrodes made by fused deposition modeling (FDM) method using a conducting carbon-filled polylactide resin composite (c-PLA) on top of the insulating layer. It demonstrates that it is possible to quickly build devices for neuromorphic performances using a hybrid of affordable and design-flexible AM techniques. The high resistance of the printed thermoplastic polymer, c-PLA, is one restriction mentioned in this paper indicating that the source and drain electrodes are currently experiencing high resistive loss. This problem leads to the lower transconductance (0.25 mS) of OECT device. Another challenge in this work is the resolution. Although it is novel to create the whole device with direct-writing techniques, large channel length and width demonstrate the limitation of 3D printing to make devices with smaller channel length [67].

Alternatively, a simple method has been developed to eliminate the mentioned disadvantages of traditional electrode materials and fabrication methods. By using a CO_2 laser, a polymeric substrate can be converted to laser-induced graphene (LIG) in a simple, low-cost way, which will be discussed in Chapter 2. In this thesis, a

study of LIG-based electrodes for OECT devices with inkjet printed semiconductor is presented.

1.6. Inkjet Printing

Electronic devices including electronic circuits, displays, and sensors can be created using printing technology. There are wide range of printing technologies that are used with the idea of an additive process. Therefore, all the circuit components and devices are fabricated by using an additive process instead of subtractive processes. The conductors and semiconductors are added where they are needed. The printing methods manage the process of depositing material ink on a substrate to create active or passive devices such as capacitors, thin film transistors, and other electronic devices [68].

Printed electronics is a fast-growing technology and demonstrates a wide range of successful applications in different industries including healthcare, automotive, consumer electronics, and aerospace. It is a low-cost method in terms of processing since it can be printed on various substrates such as plastics, papers, glass, and flexible polymers. It is an effective, quick, and simple way of fabrication technology. Different methods are used for printing technology such as gravure printing, screen printing, and inkjet printing [69].

Placing a droplet of material at the desired point is the advantage of inkjet printing. The materials can be printed which range from biologically useful cells,

biocompatible polymers, and metals such as silver, gold, and iron. Inkjet printer delivers a reproducible uniform droplet. The print head contains a piezoelectric actuator. As the voltage of piezoelectric material changes, the pressure inside the print head alters which results in the ejection of droplet. Inkjet printing has several advantages. First, the functional ink material can be printed directly through the nozzle to the substrate. Also, one of the droplets can print the large area which leads to the efficient use of ink. Very chemically sensitive materials such as DNA, and proteins can be printed via inkjet printing [70].

A wide variety of inks with intermediate surface tension and viscosity can be used with the jetting mechanism affecting the quality of printed patterns. Ink-jet printing also requires careful attention to other process variables, such as nozzle size and voltage. The final resolution of the printed feature and the size of the droplets are both influenced by the nozzle size. Additionally dependent on the applied voltage are droplet size and speed. Speed and volume rise in proportion to voltage. Yet the nozzle diameter has a significant impact on droplet size. For printing tiny features, it is advised to utilize a lower nozzle size [71]. The process of inkjet printing is shown in Figure 1-7.

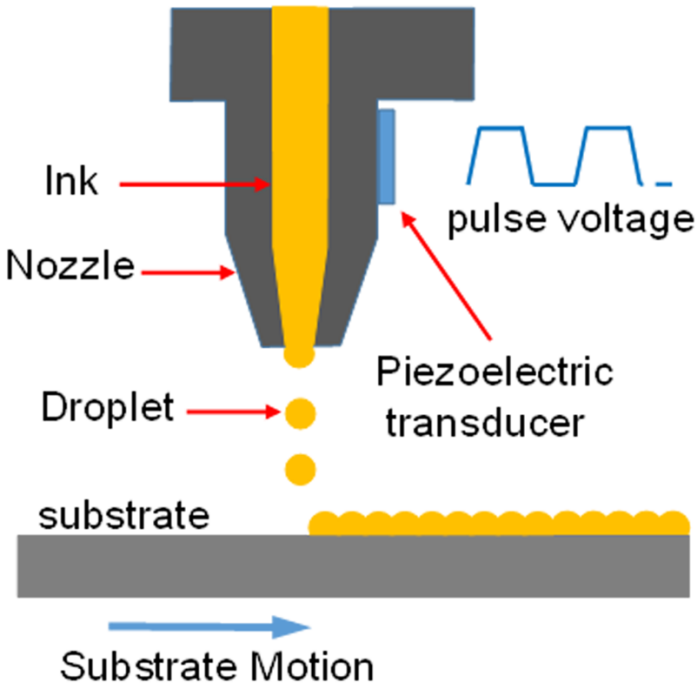

Figure 1-7. The schematic process of inkjet printing using piezoelectric material.

1.7. Integration of Electronics with 3D Printing

There are numerous ways to fabricate an object, such as casting, forming, and subtractive manufacturing. Another type of manufacturing that uses additive layer-by-layer development of the pieces is known as additive manufacturing (AM). 3D printing, which is an additive manufacturing process, enables us to construct a three-dimensional object of any shape or size from a three-dimensional model or other electronic data sources. The application of several layers of material takes place in a controlled manner by a computer [72].

Fused deposition modelling (FDM) is a procedure where thermoplastic filament is heated until it melts and is pushed out layer by layer to create a three-dimensional object. The FDM 3D printers have a support base and can move vertically. The melt extrusion method is used for extruding it layer by layer via a nozzle to create the desired object. The extruder is equipped with the ability to move in all three directions (x, y and z). Because the adjacent layers are fused together as the extruder completes the deposition, the process is known as fused deposition modelling, and the 3D printer is responsible for creating the object [72].

The incorporation of electronics into 3D printed structures has recently received a great deal of research. One of the most thoroughly researched conductive 3D printing filaments is made of thermoplastic polyurethane and carbon nanotubes

(CNT/TPU). In one study, multiaxial force sensors were made using CNT/TPU filament, with an average conductivity of 7 S/m [73].

Laser engraving of 3D printed polymeric substrate is one method to fabricate a conductive 3D printed structure. In one work, LIG pattern was fabricated via lasering the 3D-printed polymer (PEI) where a significantly lower sheet resistance (0.3 Ω/sq) than that of the commercial substrate was attained due to the physical aging of the PEI polymer during 3D printing. The LIG pattern made on 3D printed PEI was used in strain sensors resulting in very high gauge factor compared to the commercial substrates [74].

Jiao and coworkers [75] lasered a unique 3D printed substrate called ULTEM 9085. ULTEM 9085 is a combination of amorphous thermoplastics made of polyetherimide (PEI) and polycarbonate (PC) copolymers, which were used to improve flowability during the additive manufacturing process. The LIG capacitor's strong electrochemical performance was verified by cyclability testing done on 3D printed ULTEM 9085 [75].

Sensing is one of the most common applications of LIG in combination with 3D printing. A highly efficient mechanical sensor was fabricated by lasering 3D printed polyether ether ketone (PEEK) corrugated substrate. The sensitivity of strain and pressure sensors may reach 2203.5 and 678.2 kPa^{-1}, respectively, thanks to the 3D corrugated graphene structure. The expansion of the cracks for LIG shows that it

has the capacity to cause the consistent expansion of cracks. Due to the local stress concentration effect, this theory establishes that the26orrugateed microstructure is important for enhancing the sensitivity of mechanical sensors. High precision enables corrugated LIG (CLIG) sensors to distinguish between increasingly delicate signals, including pulse, swallowing, human gestures, and soft robotics movement [76].

Another type of LIG which is fabricated by lasering aromatic polysulfone-class of polymers including polysulfone (PSU), poly(ether sulfone) (PES), and polyphenylsulfone (PPSU) is called sulfur doped LIG. It has electrochemical and antibacterial properties that make it useful in different applications such as membrane filtration, fuel cells, microelectronic devices, and biomedical technology [77]. It shows remarkable thermal and chemical resistance with a very high toughness. It has high tensile strength (70 – 180 Mpa) and flexural strength (95 – 270 MPa) and its tensile modulus is very high (2500 MPa). One of the great things about PSU is its transparency which can be printed nearly 100% clear. The mentioned features make PSU a great alternative to its cheaper counterparts polycarbonate and acrylic. As a result of its higher cost, it has often only been utilized in specialized applications and is frequently substituted for ULTEM 9085 in situations where greater strength is required [78]. The incorporation of LIG to 3D-printed amorphous polysulfone substrate would make it possible to print smart

objects with extra features like sensing, actuation, or energy storage. In this thesis, the integration LIG with 3D printed PSU substrate is studied for the first time and used in different applications such as OECTs and strain sensors.

1.8. Research Objectives

In this thesis, LIG is used as an electrode in OECTS. That is because of different properties, such as high electrical conductivity and high surface area. This thesis aims to introduce a device with electrodes that can be created without any complex chemical synthesis procedures and pricy resources, and study their effect on OECT performance in terms of OFF and ON current. LIG can create a high surface area of contact with electrolytes, effectively lowering the OFF current of devices and resulting in a higher ON/OFF ratio. LIG's porosity would be helpful in the capacitive properties of devices, causing high transconductance, which is an essential parameter for this device.

To expand the applications of LIG with more complicated designs, this thesis provides an integration of electronics with 3D printing. It shows that transistors and strain sensors can be fabricated on 3D printed PSU substrates showing a good performance. Also, this material's flexibility and structure could help get increased sensitivity in strain sensors.

1.9. Thesis Organization

This thesis presents a study of graphene-based sensing devices made using inexpensive techniques. One of these devices is OECT using LIG electrodes to achieve low OFF and high ON current. By combining LIG fabrication and 3D printing techniques, a novel type of LIG based strain sensors is fabricated.

In Chapter 2, fabrication of LIG electrodes on polyimide substrate is investigated. Effect of different laser parameters on sheet resistance is studied. The properties of fabricated materials are characterised along with various pattern designs.

In Chapter 3, the inkjet printing based OECT is fabricated by using LIG as source, drain, and gate electrodes in a co-planar architecture. PEDOT:PSS is inkjet-printed as a p-type transistor's channel. Plasma treatment is used to improve the performance of the OECT devices. Channel length effect and semiconductor thickness are two parameters that are investigated in this chapter.

In Chapter 4, sulfur doped LIG is fabricated on 3D printed polysulfone which is effective in using in different applications such as OECT and strain sensor. Different mechanical and electrical tests are carried out to show the resistance changes during the mechanical test which shows how well the strain sensor works.

In Chapter 5, the main findings of this study are outlined, and recommendations for further research are given.

Chapter 2 . LASER-INDUCED GRAPHENE ELECTRODES

2.1. Introduction

Electrodes are one of the main parts of the electronic devices which play an important role in making a contact with a nonmetallic component of a circuit such as electrolyte and semiconductor depending on the type of the device. The importance of electrodes in electronic devices can be investigated from various aspects such as electrical conductivity. Moreover, some electrodes have shown flexible behaviors that makes them useful in wearable and flexible electronics [79][80]. Silver, copper gold [59], palladium [60], platinum [61] and graphene are a few of the most popular materials utilized as electrode materials.

The metallic electrodes demonstrate the excellent electrical conductivity making them as a promising material for using in the role of electrodes. However, each of them shows drawbacks such as low oxidation resistance and high cost. To mitigate these drawbacks, researchers try to find an alternative material to use as an electrode. For example, although copper shows a remarkable conductivity, it suffers from oxidation resistance which is one of the important matters in electronic devices. Moreover, platinum and palladium are cost-intensive, and they illustrate high contact resistance when in contact with organic vapors.

Graphene, which could be a substitute for metal electrodes, has garnered a great deal of interest due to its superior conductivity, high specific surface area, and large carrier mobility which paves the way for being utilized as electrodes in electronic and energy storage devices [81][82]. A straightforward technique utilizing the laser process was developed to fabricate the laser induced graphene. This chapter demonstrates LIG properties such as low sheet resistance which makes it an appropriate candidate for using in organic electrochemical transistors.

2.2. Experimental

The substrate is a flexible sheet of polyimide (PI), which is a readily available material (Kapton, 125 μm thickness). A CO_2 laser cutter device (Hydra 16A) from Hyrel 3D (Atlanta, GA) with the maximum power of 40 W was used to do laser scribing of lines and squares. The average laser power was changed via pulse width modulation. The laser process was used to laser scribe 5 mm long lines (vector mode) and 2.5 mm by 2.5 mm square shapes (raster mode) on polymer sheets. The distance between the center of two adjacent laser spots in long lines was 7.5 μm, while it was 100 μm for square as shown in Figure 2-1 (c). The reason for choosing this value is that in square there are more overlaps between LIG laser spots which needs a larger distance to avoid ablating. The design of lasering patterns is shown in Figure **2-1** (d). The nested pattern design was also used for fabricating both lines and squares which is illustrated in Figure **2-1** (e). The wavelength of the laser beam

was 10.6 μm, the laser spot was 400 μm, and the focal distance was 8 mm. For all studies, the laser power ranges between 25% and 40% with a pulse spacing of 1000 dots per inch (DPI), and the scan rate is varied between 300 and 1500 $mm.min^{-1}$. All the laser studies were conducted in ambient conditions. The laser process is illustrated in Figure 2-1.

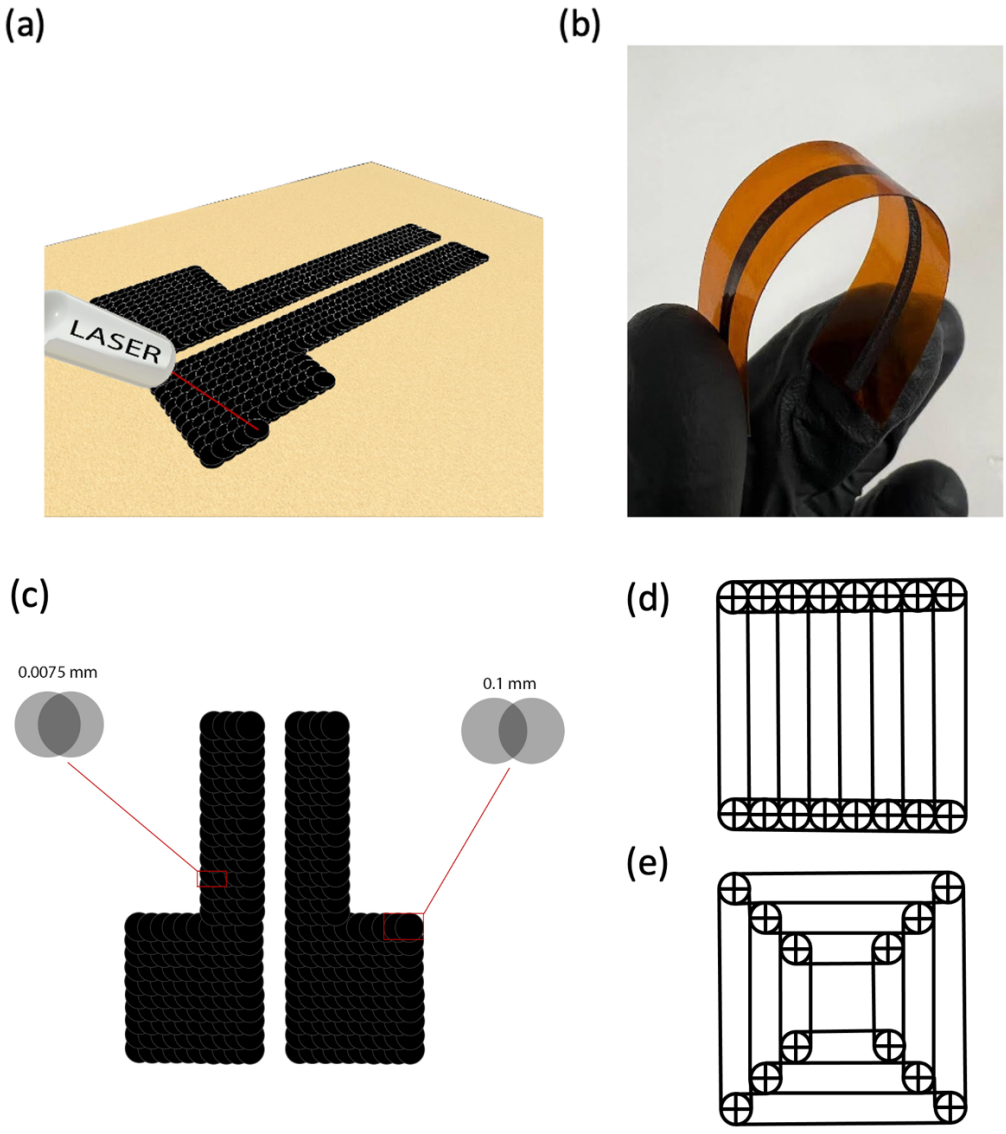

Figure 2-1. (a) Laser process on PI substrate. (b) Flexible LIG pattern on PI substrate. (c) LIG source and drain electrode shape consisting of lines and squares for contact pads. The different laser overlaps shown in two configurations; square

100 μm, and line (rectangle) 7.5 μm. (d) The laser patterning for OECT devices. (e) The nested pattern design for lasering the electrodes.

A four-point probe resistivity measuring system (Pro4, Signatone. Gilory, CA) was used to measure the sheet resistance for rectangular patterns, and a probe station with a semiconductor parameter analyzer was used to measure the sheet resistance for line patterns (Keithley 4200A). The morphology and effect of laser parameters on the porosity of engraved patterns were studied using a field emission scanning electron microscope (FE-SEM) (Thermofisher Quanta 3D). Raman spectra were acquired using a Horiba Scientific (LabRAM ARAMIS) Raman Microscope and a 532 nm laser with a laser power of 50 mW.

2.3. Effect of laser parameters on sheet resistance

In this project, the impact of laser power and feed rate was investigated for various patterns, including lines and rectangles. The power is set to a certain range, and the speed ranges from 300 to 1500 $mm.min^{-1}$. For each laser parameter in this experiment, five samples were used. Figure 2-2 demonstrates sheet resistance for lines lasered with different feed rate and power. Most of the samples show the same pattern: lowering the scanning speed and raising the laser power results in lower sheet resistance. Considering the feed rate, it is possible to determine that by raising the feed rate from 300 to 1500 $mm.min^{-1}$, the sheet resistance increases. When the feed rate is set to less than 300 $mm.min^{-1}$, the polymer primarily burns rather than

engraves, which leads to no formation of an LIG line. The feed rate of 200 mm.min^{-1} was used in this experiment, which showed that the LIG line is not created. According to the findings, 300 mm.min^{-1} is the ideal engraving speed for graphene. The lowest achieved value is 9.48 Ω/sq at feed rate of 300 mm.min^{-1} (Figure 2-2 (a)).

Moreover, by keeping the feed rate parameter constant at 500 mm.min^{-1} and increasing the laser power from 28 to 40%, 10.86 Ω/sq is the lowest sheet resistance that could be obtained (Figure 2-2 (b)). When the laser power is raised above 40%, the materials start to be ablated, and both increasing the laser power and lowering the feed rate reduce the chance of forming LIG. Also, by decreasing the laser power to less than 28%, the laser is not able to engrave and create an LIG line. Based on the work done on the correction factor in four-point probe colinear [83], the sheet resistance was calculated using Equation (2-1) where R_S stands for sheet resistance, R for resistance, L for length, and W for width.

$$R_S = \mathrm{R} \times \frac{\mathrm{W}}{\frac{\mathrm{L}}{3}} \times C' \tag{2-1}$$

In terms of correction factor C', we consider a four-point probe on a rectangular sample with the dimensions of W (width) and L (length). The probes are arranged symmetrically with point spacing of L/3. Since the ratio between W and L/3 is small

around 0.12, the sheet resistance is calculated using Equation 2-2). The results obtained through Equation 2-2) are represent in Figure **2-2**.

$$R_S = \mathrm{R} \times \frac{\mathrm{W}}{\frac{\mathrm{L}}{3}} \qquad 2\text{-}2)$$

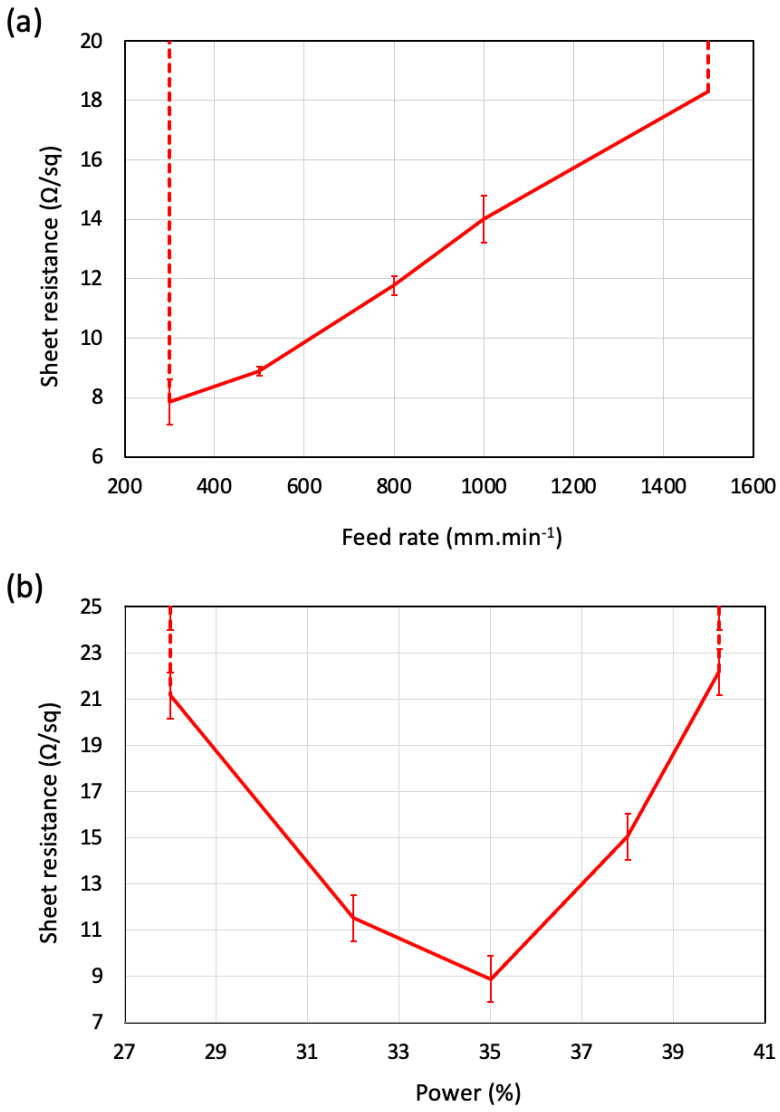

Figure 2-2. The effect of feed rate (a) and power (b) on sheet resistance for square shape. The feed rate of 500 mm.min^{-1} and power of 35 % are held constant.

Since the gate electrode has a square shape, the Van der Pauw method has been used to measure the sheet resistance. Based on the work related to measuring the correction factor for Van der Pauw method [84], sheet resistance was calculated

using Equation 2-3), where R_1 and R_2 are the resistance measured in vertical and horizontal directions using the probe station.

$$\exp\left(-\frac{\pi R_1}{R_s}\right) + \exp\left(-\frac{\pi R_2}{R_s}\right) = 1 \qquad 2\text{-}3)$$

Due to the symmetric geometry, R_1 and R_2 are equal. Hence, Equation 2-4) was used for calculating the sheet resistance for square geometry for the gate electrode.

$$R_s = \frac{\pi}{ln(2)} \times \frac{V}{I} \qquad 2\text{-}4)$$

Figure 2-3 depicts how feed rate and power affect sheet resistance in a square shape. In terms of feed rate, the sheet resistance increases by increasing the feed rate from 300 to 1500 mm.min^{-1}. The feed rate of 300 mm.min^{-1} and power of 35% result in the lowest sheet resistance of 7.86 Ω/sq. The standard deviation was used for presenting the error bars. Regarding the power, it is indicated that power 35% has the lowest sheet resistance of 8.15 Ω/sq.

To compare the difference in sheet resistance of lines and squares, the plot includes both of these shapes shown in Figure 2-4. It has been demonstrated that sheet resistance of the square is lower than the line in most of the power and feed rates, which can be due to more pulse overlapping in the square shape. With larger power, the sheet resistance increases because of LIG ablation.

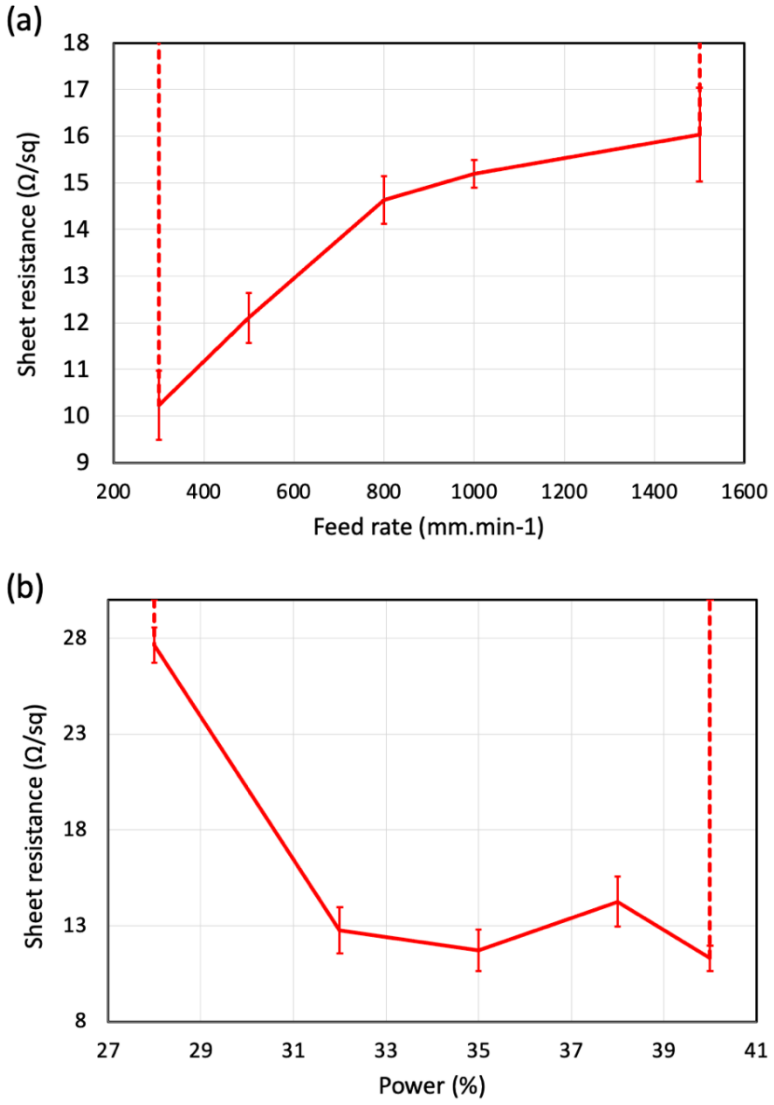

Figure 2-3. (a) Sheet resistance measurements for lines with power 35% and different feed rates. (b) The effect of laser power on sheet resistance for lines. The feed rate of 1000 mm.min^{-1} and power of 35 % are held constant. With increased power, sheet resistance decreases until the material is ablated.

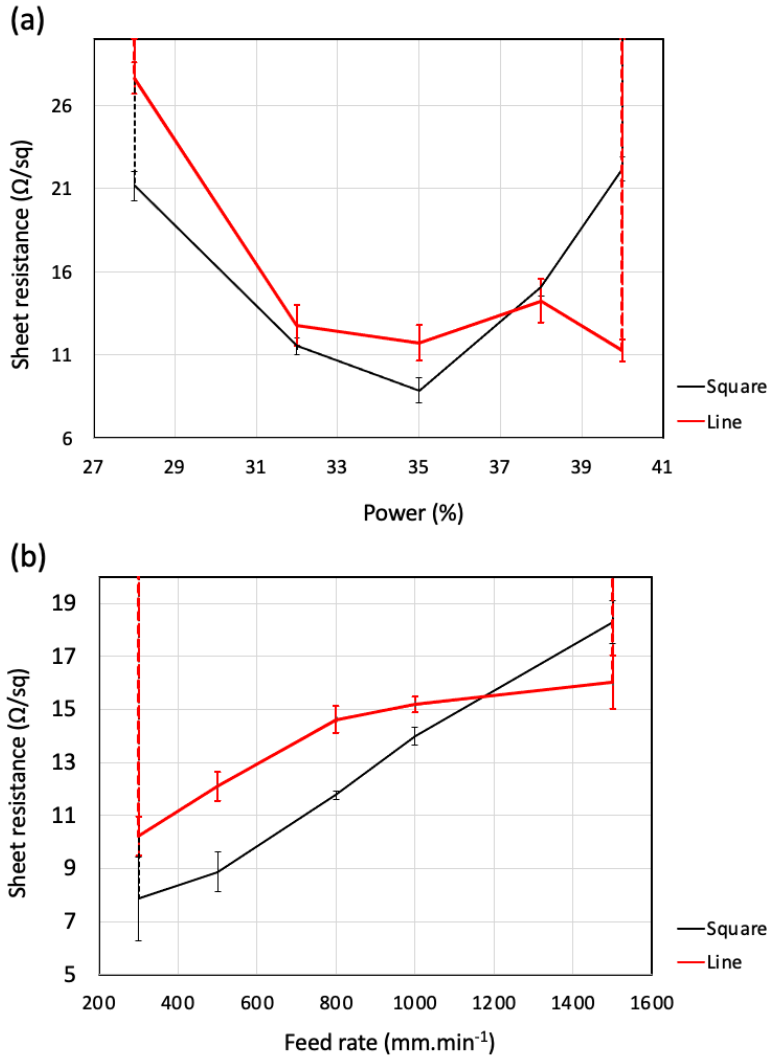

Figure 2-4. Effect of both (a) power and (b) feed rate on sheet resistance of line and square shapes.

2.4. Material Characterization

2.4.1 SEM

SEM images of the LIG surface were taken for investigating the morphology and the porosity characteristic of LIG. As shown in Figure **2-5**, different laser power and feed rate at low magnification were taking into consideration for observing the variety of morphology and porosity. Since gaseous release plays an important role in making the porous LIG structure [31][36], there would be a relation between laser parameters and gaseous release.

It seems that at higher feed rates, due to the shorter time for heat to accumulate, there is not much gas release; however, because of the longer time for heat to accumulate at lower speeds, less gas is released from the structure which creates the low porosity structures as shown in Figure **2-5**. It is clear in Figure **2-5** © that high feed rates do not allow enough time for the gases to be released out of the structure and make the porous morphology, while it happens in the lower feed rate like 300 $mm.min^{-1}$.

Furthermore, at lower power, it can be seen that there is not enough power to generate the essential heat leading to the gaseous release from the structure, while the larger power could be potentially helping to increase porosity as long as the material is not ablated. The relation of laser power and gaseous release and effect of them on the porosity formation of LIG are shown in Figure **2-6**. It is illustrated

that power of 40% is able to generate the heat that can help the release of gases easily and make the porous structure which is not applicable to power of 28%.

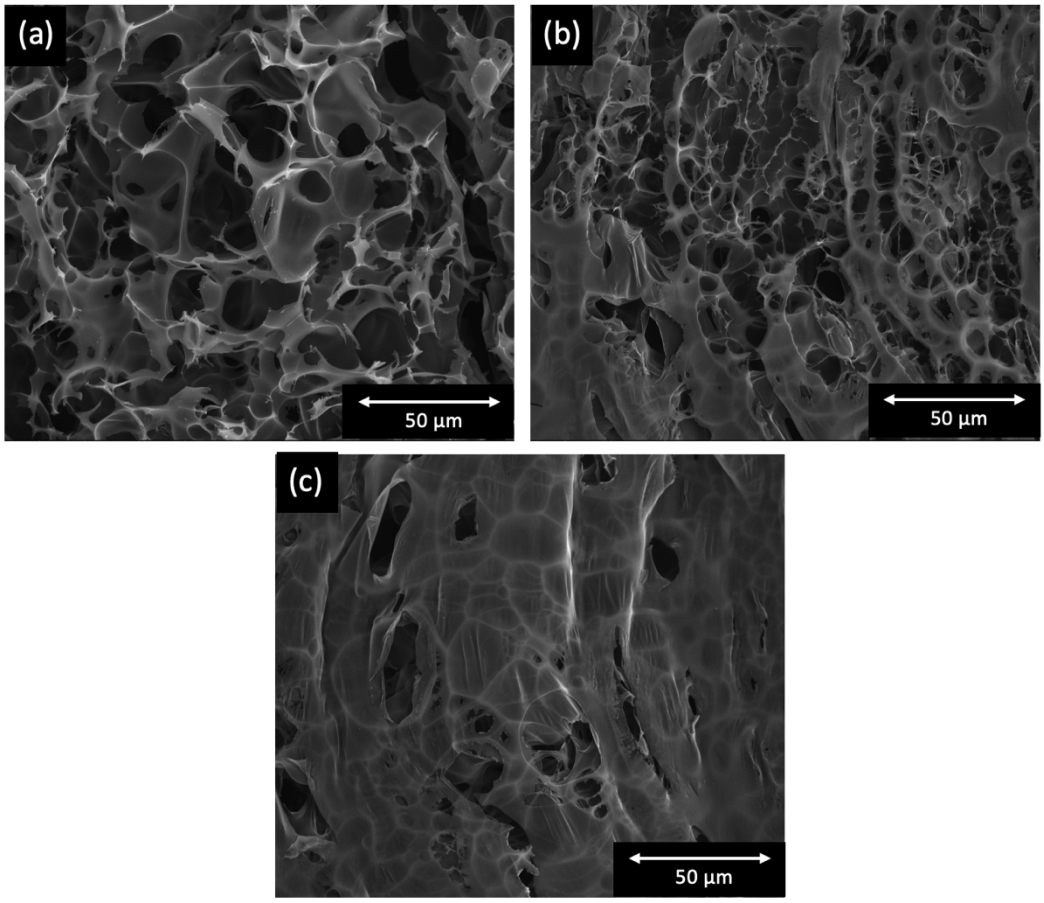

Figure 2-5. The effect of different feed rate (a) 300 mm.min^{-1}, (b) 1000 mm.min^{-1}, and (c) 1500 mm.min^{-1} on gaseous release and porous LIG formation.

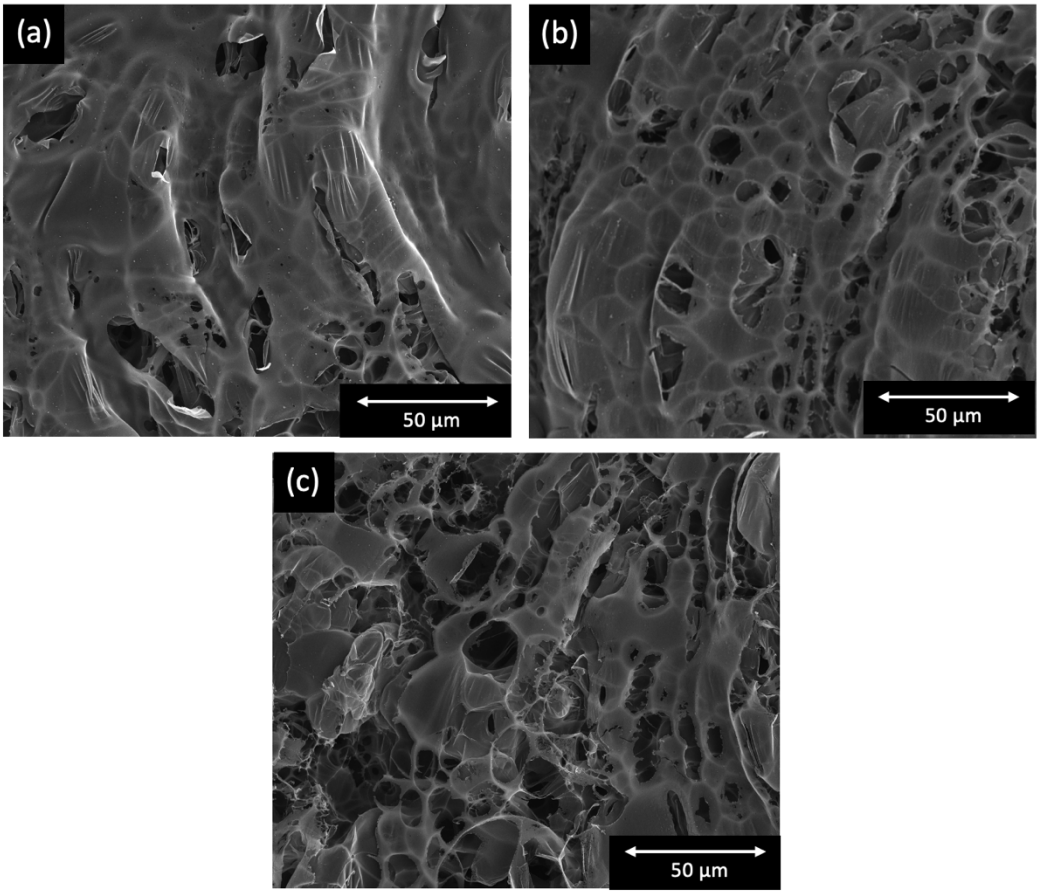

Figure 2-6. As power increases from (a) 28% to (b) 32%, and (c) 40%, the gas releases resulting in porosity formation of LIG.

To further investigate the porosity of LIG, Figure **2-7** shows the morphology of line shapes of LIG for different laser power and feed rate at lower magnification. As shown in Figure **2-7** (a), (b), and (c), LIG morphology is more porous with lower feed rates of 300 and 500 $mm.min^{-1}$ compared to 1000 $mm.min^{-1}$ by keeping the power of 35% constant for the experiment. This difference is also observed for

different powers where the porosity of LIG with the power of 35% is larger than for powers 32 and 28% with constant feed rate of 1000 mm.min^{-1}. Hence, by decreasing the feed rate and increasing the power, highly porous LIG is achieved until the material is ablated. This effect is much clearer for lines since there are not any overlaps as in squares affecting the morphology of LIG. As shown in Figure 2-8, the image analysis by ImageJ software was used for the sample with power of 35% and feed rate of 500 mm.min^{-1} to show the pore size and distribution.

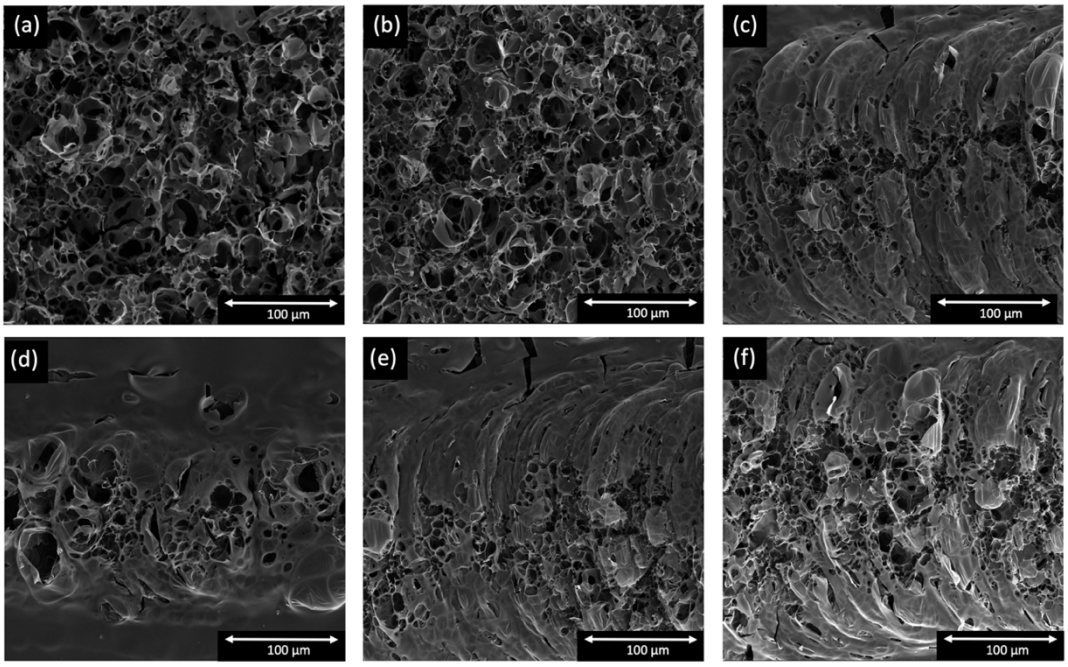

Figure 2-7. SEM images of the LIG surface of line shapes with low-magnification a) 300, (b) 500, (c) 1000 mm.min^{-1} laser feed rate, and d) 28, e) 32, and f) 35 % laser power on PI substrate. The power of 35% and feed rate of 1000 mm.min^{-1} are held constant, respectively.

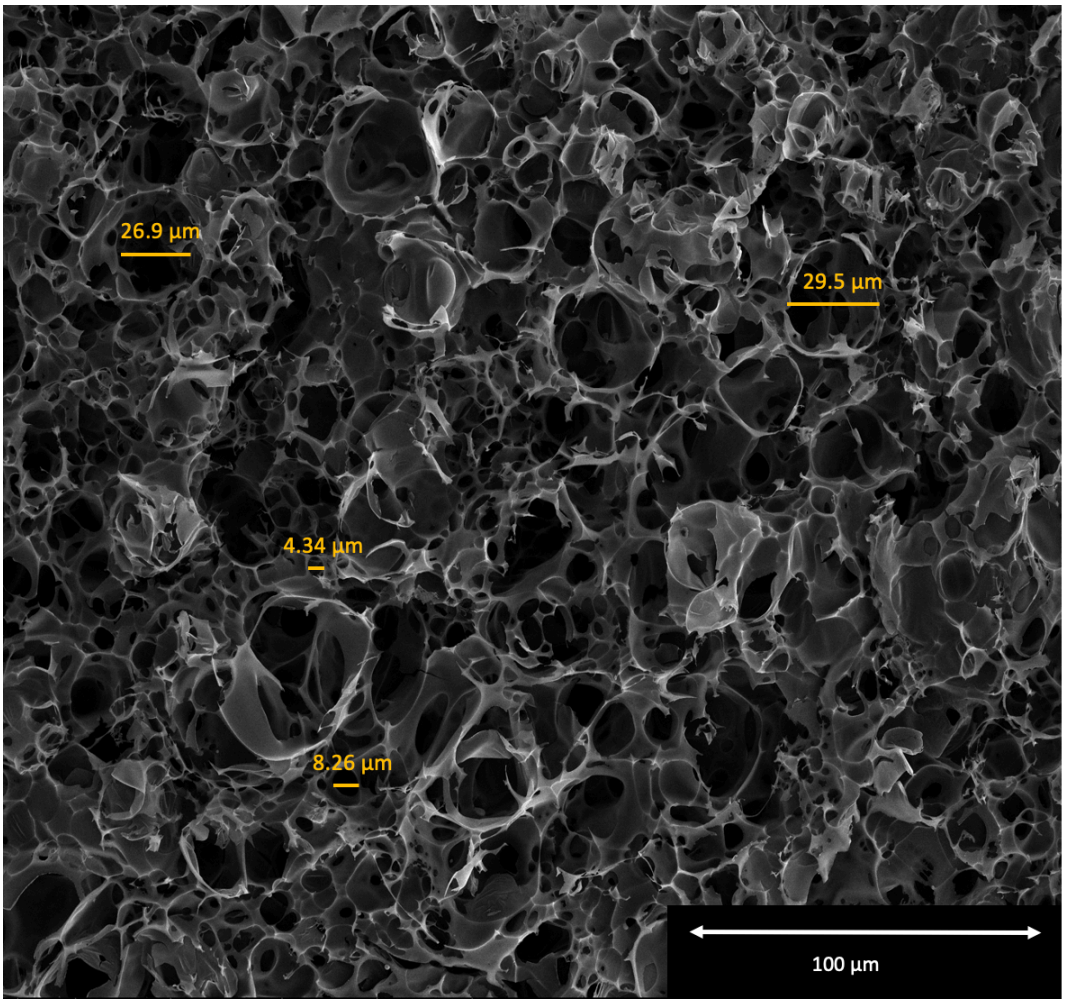

Figure 2-8. Illustration of pore size and distribution for the sample using ImageJ software. The power of 35% and feed rate of 500 $mm.min^{-1}$ was used for this sample.

2.4.2 Raman Spectroscopy

Raman spectroscopy is used to investigate the presence and quality of the LIG material on a substrate. Raman spectroscopy, known as a non-destructive technique,

is a vibrational characterization method that is based on the sample's inelastic scattering of light in the visible or near-infrared range. It is an effective method for keeping track of how graphitized material changes structurally.

In Figure 2-9, the Raman spectrum is shown for the sample with feed rate of 1500 $mm.min^{-1}$ and power of 35%. It is possible to identify the presence of graphene due to the existence of graphene's distinctive peaks. The D, G, and 2D peaks appear at wavenumber of 1350, 1550, and 2700 cm^{-1}, respectively, indicating the presence of multi-layer graphene. These Raman peaks can be used to determine various graphene structural characteristics. The 2D peak denotes the creation of multi-layered graphene, while the D peak represents the LIG defects concentration or the disorder in the sp^2 hybridized structure of the carbons in graphene. The most significant peak for graphene or graphite, commonly known as the graphitic peak, is the G band [38][74].

In addition to the mentioned important peaks, the full width at half maximum (FWHM) of the 2D peak could also demonstrate some information related to the LIG. A broad FWHM in 2D peak identifies more layers in the graphene-like structure. This value rises when more graphene layers are added. The I_D/I_G ratio represents the quality of graphene and number of disorders, while I_{2D}/I_G ratio demonstrates that the LIG contains multiple graphitic layers.

Position in relation to the laser pulse affects the quality of LIG, and some regions with 38% power show good quality graphene. The spectrum, which was acquired from a different location on the sample, exhibits a sharp 2D peak at 2700 cm^{-1}.

D and G bands are seen in all samples at 1300 cm^{-1} and 1550 cm^{-1}, respectively. However, the 2D peak intensity is not very high and it is just a broad peak for the sample with feed rate of 800 $mm.min^{-1}$ shown in Figure 2-10. The interconnecting peak made up of the D and G bands, which are not separated, is high-temperature annealed nano graphite.

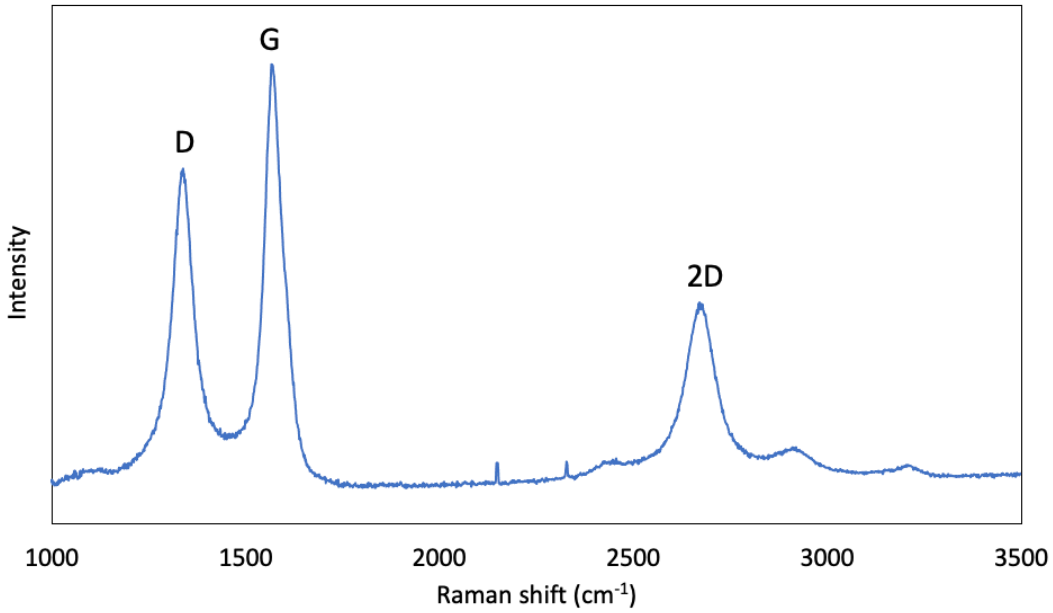

Figure 2-9. Raman spectrum of laser-induced graphene fabricated on PI with the laser feed rate of 1500 $mm.min^{-1}$ and power of 38%.

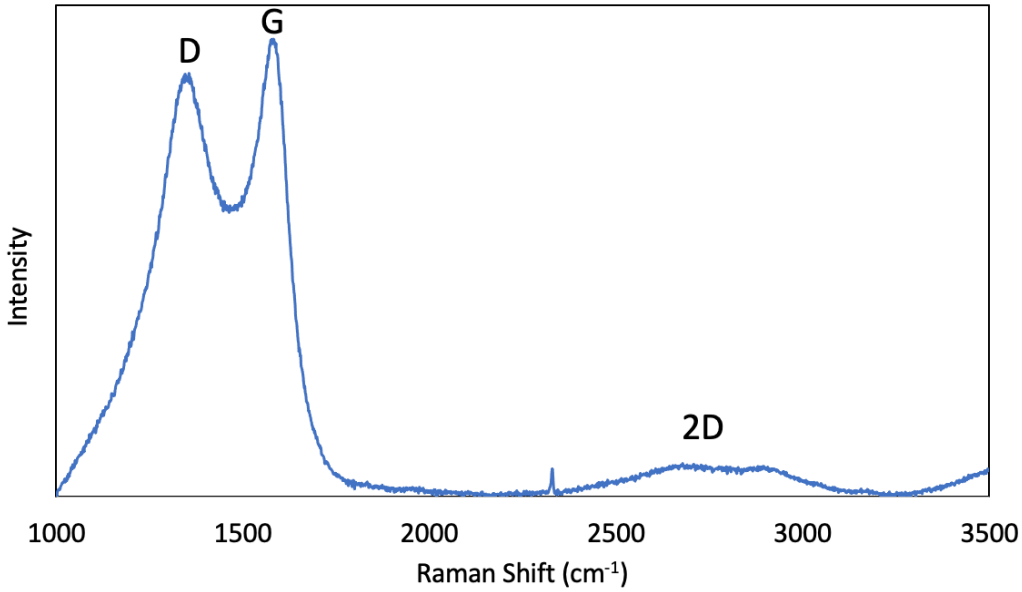

Figure 2-10. Raman spectrum of laser-induced graphene fabricated on PI tape with the laser feed rate of 800 mm.min^{-1} and power of 35%. The broad 2D peak is happening at Raman shift of 2700 cm^{-1}.

During the fabrication of LIG on polyimide tape, a boundary around the LIG line is constructed due to the laser power and feed rate, which could be wrongly assumed that this area is also LIG shown in Figure 2-11 (a). Since the color of that region is quite similar to the LIG line itself, this area is investigated via Raman spectroscopy. As shown in Figure 2-11 (b), Raman test demonstrated that the LIG is not fabricated in that area. Also, the Raman spectrum for polyimide is shown in Figure 2-11 (c).

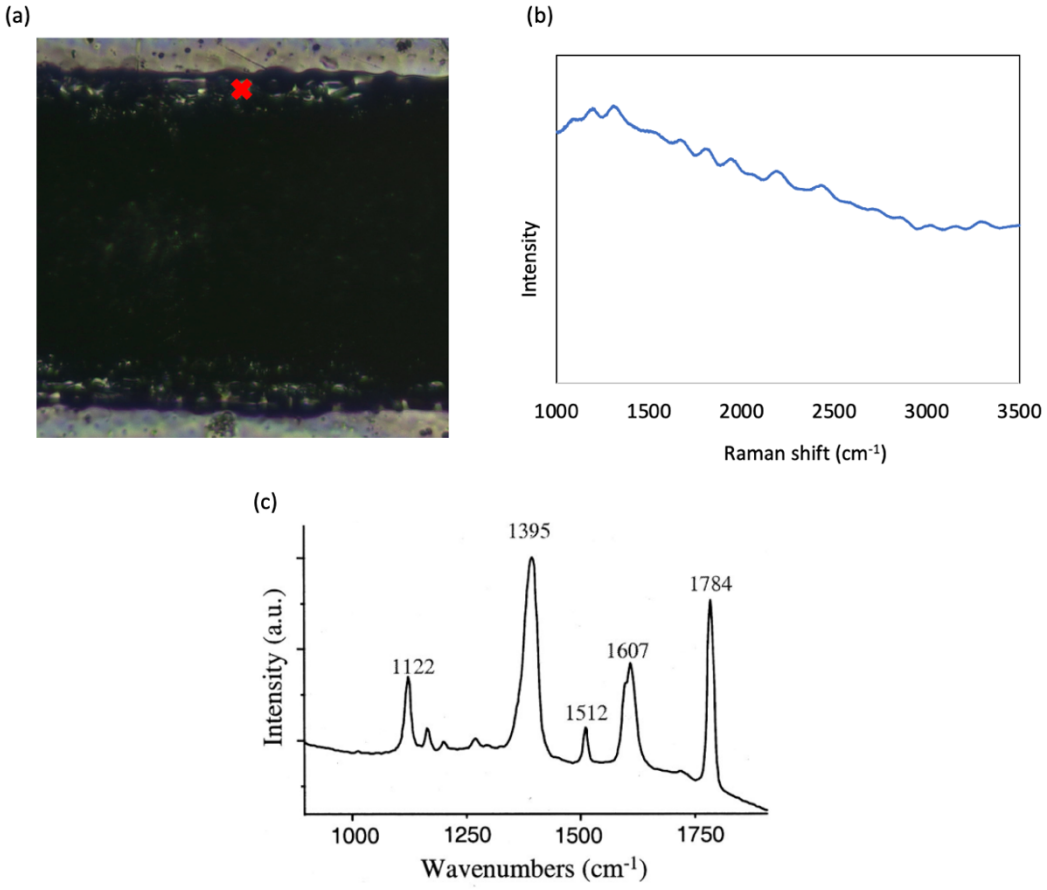

Figure 2-11. The proof showing that there is no LIG in the boundary around the line. (a) The microscopic image illustrates the boundary region which is not LIG. (b) The Raman diagram shows there are no peaks at 1350, 1550, and 2700 cm^{-1} that would prove the formation of LIG in the boundary area. (c) Raman spectrum of PI.

2.5. Conclusion

We have used a CO_2 laser to show how a polyimide polymer can be directly converted into graphene. The laser power and feed rate were adjusted to get the lowest sheet resistance. Increasing power and reducing feed rate minimises sheet resistance and defect density until the material is ablated. The minimum sheet resistance of 7.86 Ω/sq achieved for the square patterned electrodes with the laser power of 35% and feed rate of 300 $mm.min^{-1}$. Also, in terms of morphology, highly porous LIG is produced by reducing the feed rate and raising the power until the material is ablated. This technology makes it simple to create highly conductive electrodes, which opens up a wide range of applications.

Chapter 3 . LIG BASED ORGANIC ELECTROCHEMICAL TRANSISTORS (OECTS)

3.1. Introduction

Organic electrochemical transistors (OECTs) are a type of OFET and similar to the electrolyte-gate OFET in which the ions of electrolyte can go into the semiconductor inducing much more electronic charge. Unlike OFETs, there is no insulator between semiconductor channel and electrolyte. The key difference is that in OFET and electrolyte-gated OFET, the electronic charge is very close to the surface; therefore there is a very thin layer next to the interface with electrolyte or the interface with dielectric. However, in OECTs bulk doping occurs in the semiconductor channel. The field effect happens in the bulk of material. OECT contains an insulating substrate, source and drain electrodes and film of semiconductor which is in contact with an electrolyte. In general, one of the advantages of OECT compared to OFET is its amplifier behavior that can amplify a small input signal and provide large output currents with low operating voltage. Stability in aqueous solution is another advantage of OECT. An OECT can also act as a transducer by detecting a change in electrochemical potential.

Although there are several materials such as gold [85], silver [86], and platinum that have been used as electrode materials, there are still some challenges including the high cost and complicated fabrication process. Recently, LIG is achieved by lasering polymeric substrates and used for supercapacitors, an electrocatalyst for fuel cells, radio-frequency identification (RFID) antennas, biological sensors, among other potential applications. Here, in this report, LIG has been used as all electrode materials of OECT for the first time. Not only the method of LIG fabrication is very easy, but also because of its large surface area, it is possible to increase the capacitance of gate electrode which improves the transistor performance [62].

3.2. Experimental

3.2.1. Electrode design and fabrication

A flexible sheet of the material polyimide (PI), which is widely accessible (Kapton, 125 μm thick), serves as the substrate. On polymer sheets, 5 mm long lines (vector mode) and 2.5 mm by 2.5 mm square forms (raster mode) were laser scribed using a 40 W CO_2 laser cutter (Hydra 16A) from Hyrel 3D (Atlanta, GA). Long source and drain lines had a laser pulse overlap of 7.5 μm, compared to 100 μm for square contacts and the gate. Both squares and lines were also made using the spiral mode. The laser's focal distance was 8 mm, its wavelength was 10.6 μm, and the laser's spot size was 400 μm. All experiments use lasers with a power range of 25% to 40%, a pulse spacing of 1000 dots per inch (DPI), and a scan rate range of 300 to 1500 $mm.min^{-1}$. The entire laser research was done in ambient conditions.

3.2.2. OECT device fabrication

A glass carrier was employed below the Kapton tape, which has a thickness of 125 μm. Figure **3-1** (a) illustrates the device architecture. Directly lasered in two parallel lines on Kapton tape were the LIG source and drain electrodes. Because the electrolyte will be on top of the source, drain, and gate electrodes in this layout, two 2.5 mm by 2.5 mm LIG squares were scribed as contact pads and attached to the bottom of the source and drain electrodes in order to conduct electrical probing

without coming into contact with the electrolyte. Furthermore, in a co-planar layout, the gate electrode's square is lasered with the same dimensions as the contact pads next to the source and drain electrodes. Since LIG is a hydrophobic material, an air plasma treatment was carried out (March Instruments Inc., Concord, CA) using 50 W of power and a 40 second duration for the gate electrode to maximize the contact surface of electrolyte with the gate electrode.

Regarding the ink preparation for the semiconductor channel, 6 wt% ethylene glycol (EG, Sigma Aldrich) and 0.1 wt% dodecyl benzene sulfonic acid (DBSA) were added to commercial 1.3 wt% PEDOT:PSS aqueous dispersion in H_2O (Clevios PH 1000, Hereaus) to improve the morphology and jettability of the ink ,respectively. Additionally, to render PEDOT:PSS films insoluble in aqueous solutions, 1 wt% (3-glycidyloxypropyl) trimethoxysilane (GOPS) was used to cross-link the materials. All of these enhancements generally increase the electron and ionic conductivity of the semiconductor layer in the transistors. In order to remove any remaining agglomerated particles, the ink was lastly filtered. A RheoSense VISC Portable Viscometer (RheoSense Inc., San Ramon, CA) was used to measure the ink's viscosity at room temperature.

Since the architecture is co-planar and all the electrodes are in the same plane, inkjet printing was used to deposit the semiconductor materials. The thickness of semiconductor is controllable by using inkjet printing. Using a specially created

piezoelectric drop-on-demand (DOD) inkjet printer, the semiconductor ink was printed in a rectangular pattern on top of the source, drain, and transistor channel. Any design can be printed using a LabVIEW application (National Instruments, Austin, Texas), by adjusting the printer stage's position in relation to the printhead. The orifice diameter of the Microfab Technologies, Inc. (Plano, TX) nozzle (type B21- 101-02) is 60 μm. Printing a line requires a drop spacing of 65 μm, whereas a rectangle requires a drop spacing of 30 μm between each line. Ink-jet printing requires clean, flat surfaces with minimal roughness. Since PEDOT:PSS is a water-based p-type semiconductor, it can hardly be deposited on polyimide tape between LIG source and drain electrodes due to its hydrophobic nature. Therefore, a plasma treatment with power of 50W for 40 seconds is helpful for making the polyimide tape more hydrophilic resulting in the uniform layer of PEDOT:PSS.

The printed pattern was then placed on a hot plate and dried for 20 minutes at 120 °C. The electrolyte was then dropped onto the source, drain, and gate electrodes in the amount of 40 μl of NaCl solution in water at a concentration of 100 mM. The whole OECT device is shown in Figure **3-1** (b).

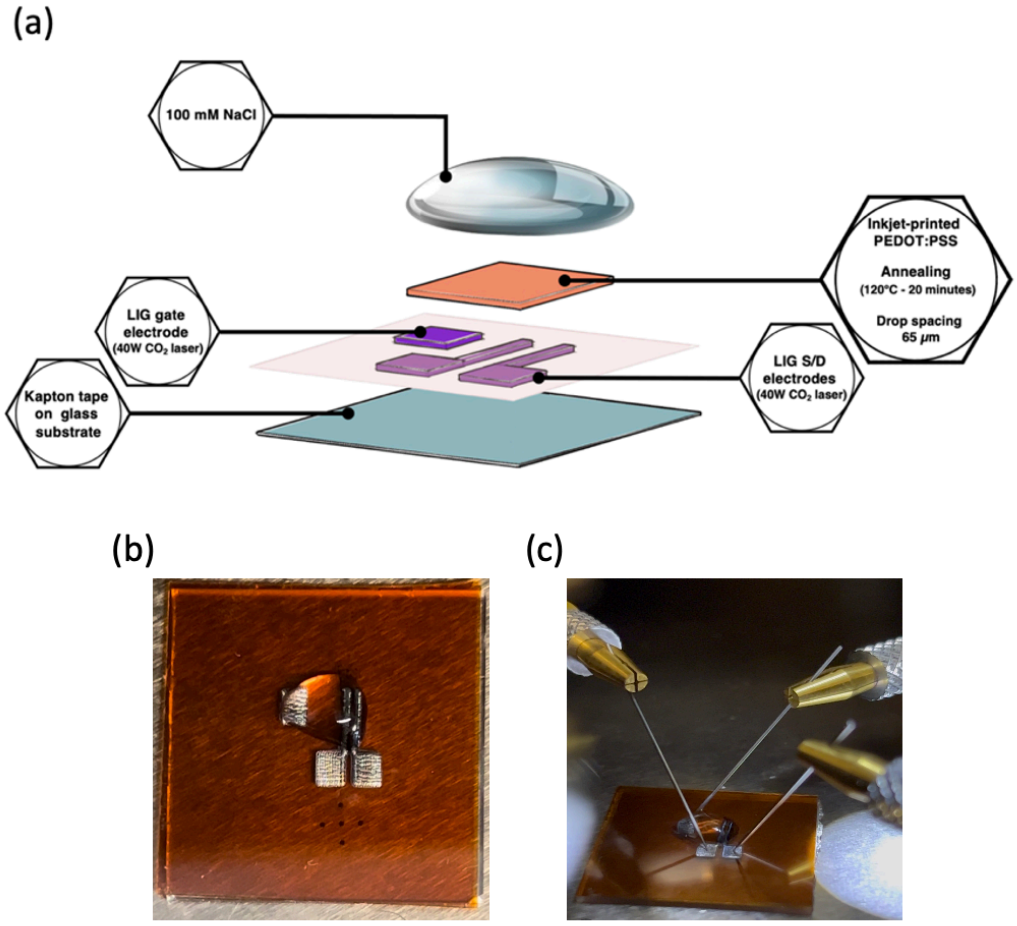

Figure 3-1. (a) Schematic of the architecture of LIG-based OECTs. (b) Photo of the fabricated OECT device with LIG electrodes. (c) LIG-based OECT during the electrical measurement.

The bipolar waveform parameters that are applied when jetting PEDOT:PSS ink using an inkjet printer are shown in Table 3-1. To avoid the satellite effect, these variables are essential. When in satellite development, the droplet separates from the main droplet and develops a long tail before disintegrating into a little droplet. Satellite droplets will deteriorate print quality and pattern definition. The ink stream jetting from the nozzle aperture is depicted in Figure **3-2**. It shows the formation of spherical droplets without the presence of a secondary droplet. The rectangle pattern of PEDOT:PSS on top of the channel, source, and drain electrodes is shown in Figure **3-3**.

Table 3-1. The settings for jetting PEDOT:PSS ink that are utilized in inkjet printing.

Parameter	**Value**
Rise time 1 (μs)	12
Dwell time (μs)	20
Fall time (μs)	12
Echo time (μs)	40
Dwell voltage (V)	34
Echo voltage (V)	-34
Idle voltage (V)	0
Rise time 2 (μs)	12

Figure 3-2. The satellite-free production of spherical droplets and a stream of ejected PEDOT:PSS ink.

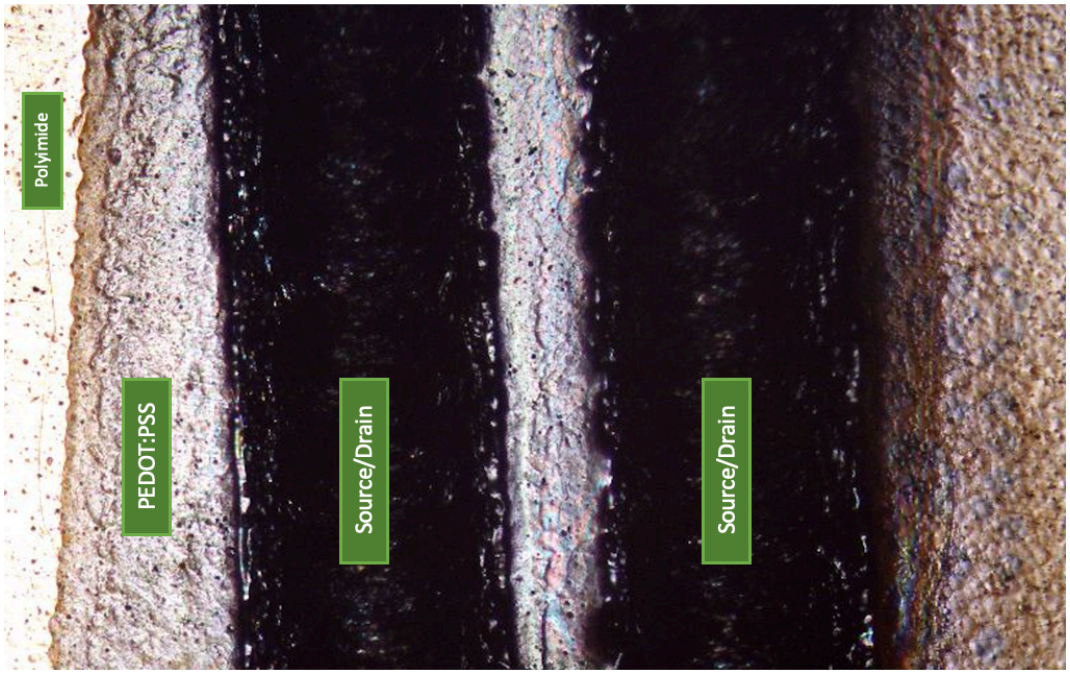

Figure 3-3. PEDOT:PSS as a semiconductor channel is shown deposited via inkjet printing. Printing a line required a drop spacing of 65 μm, whereas a rectangle required a drop spacing of 30 μm between each line.

3.2.3. OECT device characterization

The thickness of a semiconductor channel was measured using optical profilometry (Bruker contour gt-k, Billerica, MA). The transfer and output characteristics were measured using a Keithley 4200A semiconductor parameter analyzer as shown in Figure **3-1** (c). By varying the gate voltage from 1 V to -1 V in steps of 0.02 V while maintaining a constant drain voltage of -1V, the transfer curves (Id-Vg curves) are observed. The output characteristics (Id-Vd curves) are generated by varying the applied gate voltage while sweeping the drain voltage from 0 V to -1 V in steps of 0.005 V. This method was carried out for Vg by sweeping from 1 to -1 V in increments of 0.5 V. The devices were initialized by performing the transfer measurement twice before recording the transfer curves presented here.

3.3. OECT I-V characteristics

A transfer curve for the LIG-based OECT without plasma treatment of the gate is shown in Figure **3-4** (a) in the saturation regime. Laser power and feed rate parameters were all the same for source, drain, and gate electrodes configured at 35% and 500 mm.min^{-1}, respectively. As shown in Figure **3-4** (a), the magnitude of the drain current reduces as V_g becomes more positive for a constant $V_d = -1V$. The anti-clockwise hysteresis related to slow ion migration in the double sweep measurements is very small. As shown in Figure **3-4** (a), the OFF current is 0.395 mA. The ON current and ON-OFF ratio for the mentioned device is 3.62 mA and

9.16, respectively. Depletion mode is demonstrated in this transistor. Transconductance, $g_m = \frac{\partial I_d}{\partial V_g}$, of 1.77 mS was achieved.

The output characteristics are presented in Figure **3-4** (b). The channel current exhibits a linear relationship with V_d at low drain voltages and saturates at higher V_d levels for various V_g values. The channel was virtually shut off after applying a gate voltage of +1V. This turn-off voltage is far lower than many other transistor technologies. However, as demonstrated in Figure **3-4** (a) and (b), the transistor is not completely off.

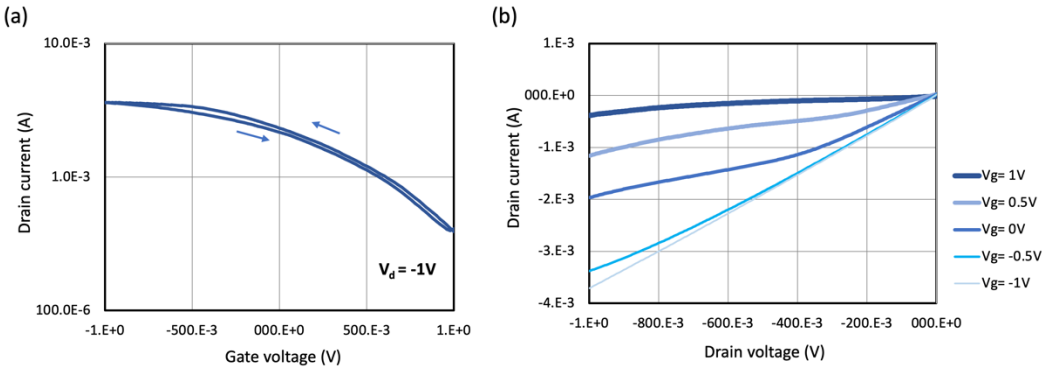

Figure 3-4. a) Transfer and (b) output curves of LIG-based OECTs without plasma treatment of the gate.

The contact of the gate electrode with the electrolyte on top is one of the key elements in enhancing the performance of the generated OECTs, particularly in terms of OFF current and ON-OFF ratio. For this purpose, the gate electrode was

plasma treated for 40 seconds at a power of 50 W. The hydrophobic LIG gate electrode became hydrophilic as a result of this. The transistors can have a significantly lower OFF current due to the improved contact with the NaCl electrolyte. Also, this plasma treatment process of the gate results in increasing the area of grate which is in contact with the electrolyte. Since the largest fraction of the applied V_g drops across the smallest capacitor, plasma treatment can make the most of voltage drops at the interface of electrolyte and semiconductor which helps improvement of OECT parameters such as transconductance. As shown in the transfer and output characteristics in Figure **3-5** (a) and (b), OFF current of 0.035 mA, ON current of 2.56 mA, and ON-OFF ratio of 72.80 was achieved. This device has a transconductance that is more than 2 mS and comparable to OECTs that have been reported in the literature [62][87]. The threshold voltage was 0.444 mV (Figure **3-5** (c)).

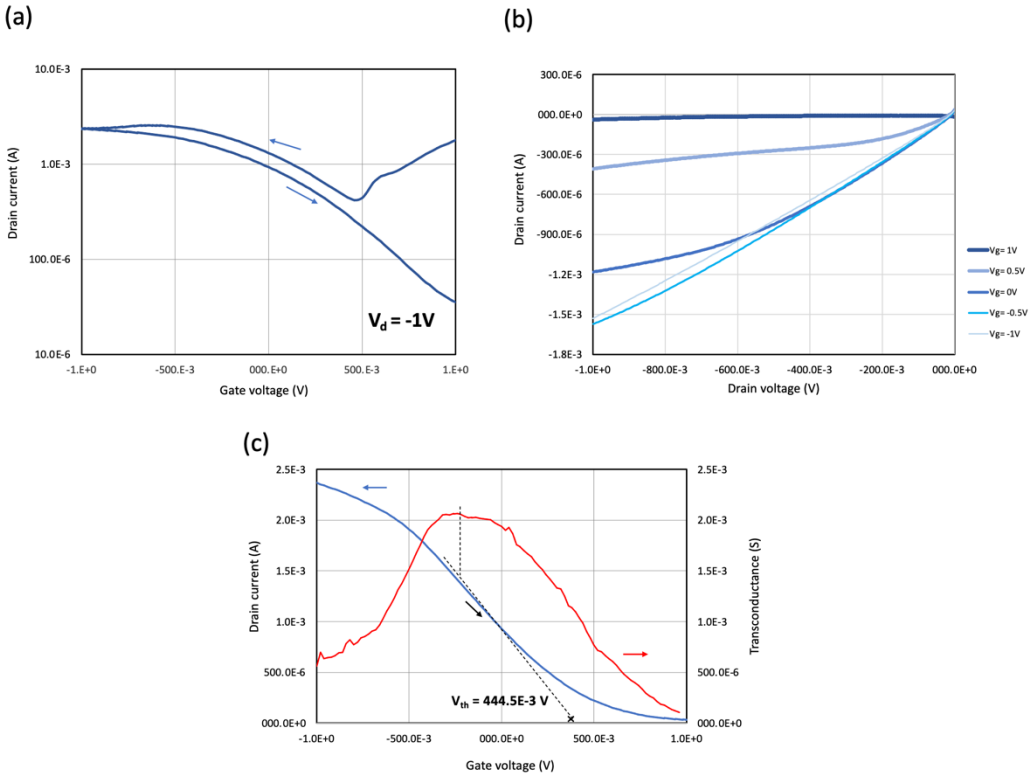

Figure 3-5. (a) Transfer curve of OECT with a plasma treated gate electrode. (b) Output characteristics of LIG based OECT with a plasma treated gate electrode (c) Transconductance versus gate voltage for the OECT with plasma treated gate electrode (Laser power of 35% and feed rate of 500 mm.min^{-1}).

3.3.1. Effect of semiconductor thickness on OECT performance

It is crucial to take into account the semiconductor channel's thickness when inkjet printing. The thickness of the semiconductor channel in the transistor channel, between the source and drain electrodes, were measured using optical profilometry,

as shown in Figure **3-6**. The data indicate that the PEDOT:PSS channel is approximately 1500 nm thick. In order to look into the thickness difference of the semiconductor material created using inkjet printing, the investigation was done to show how much thicker the PEDOT:PSS layer is outside of the electrode region than the thickness of the material that was deposited between the LIG electrodes.

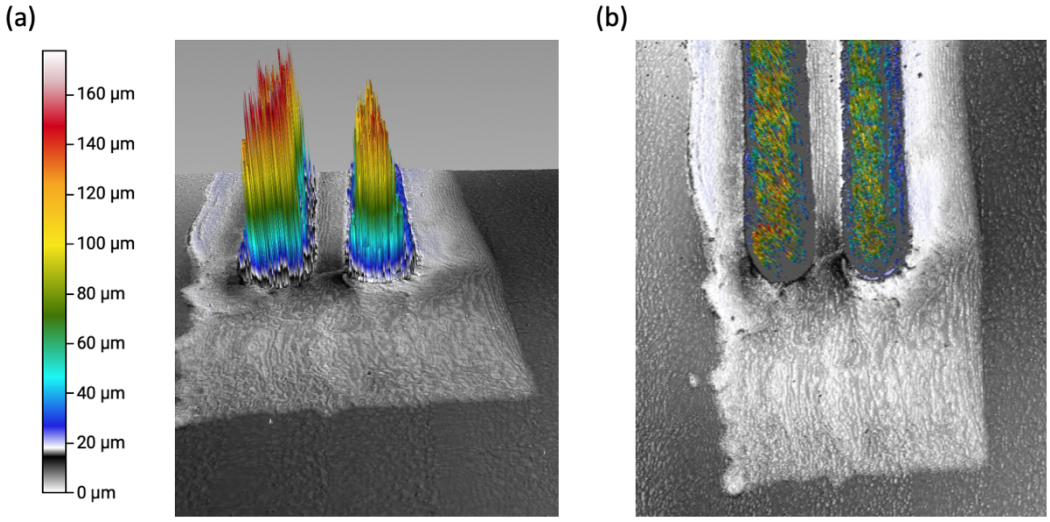

Figure 3-6. (a) Thickness measurement using profilometer of LIG electrodes and PEDOT:PSS semiconductor channel on PI substrate. (b) 2D plot of electrodes and semiconductor channel.

Transistors were created with one, two, and three inkjet-printed layers of semiconductor to examine the impact of semiconductor layer thickness on OECT performance. As seen in Figure **3-7**, increasing the number of layers of semiconductor material increases both OFF and ON current. Both ON and OFF

current follow and increasing trend as anticipated given the physics of the device. In OECTs, ions travel throughout the whole thickness of the semiconductor, in contrast to MOSFETs where charges create the channel at the interface between the dielectric and semiconductor. As a result, the hole current can flow through a thicker semiconductor layer as the semiconductor channel thickness increases, which results in a larger ON-current. All other experiments shown in this thesis have the semiconductor thickness equal to one layer of PEDOT:PSS.

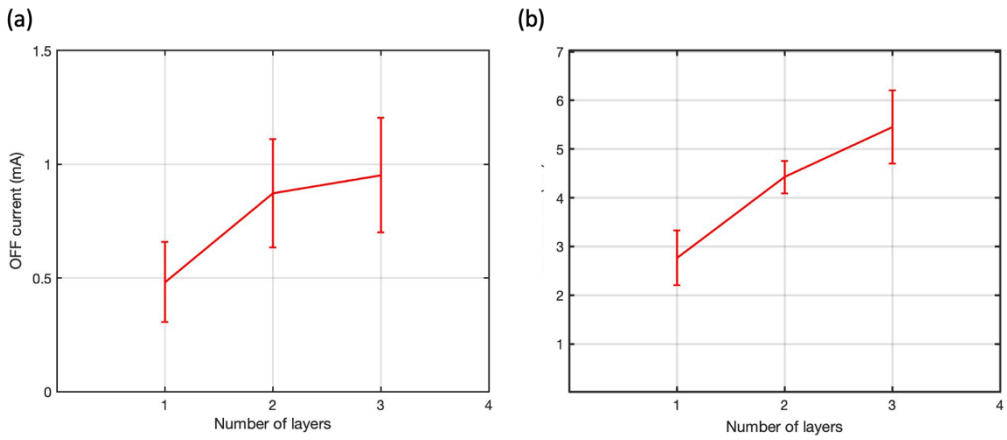

Figure 3-7. Effect of semiconductor layer thickness on (a) OFF and (b) ON current of OECT.

3.3.2. Channel length effect

The channel length is one of the variables that influences the I-V characteristics. To see the effect, the OECT is constructed with various channel lengths including 150 μm, 190 μm, 310 μm, 410 μm, and 510 μm. Drain current in saturation mode is inversely correlated with channel length for long-channel devices, and longer channel lengths result in lower drain current. As shown in Figure **3**-**8**, the maximum ON current is 6.76 mA, which is for channel length of 150 μm. As the channel length increases, less ON current is achieved.

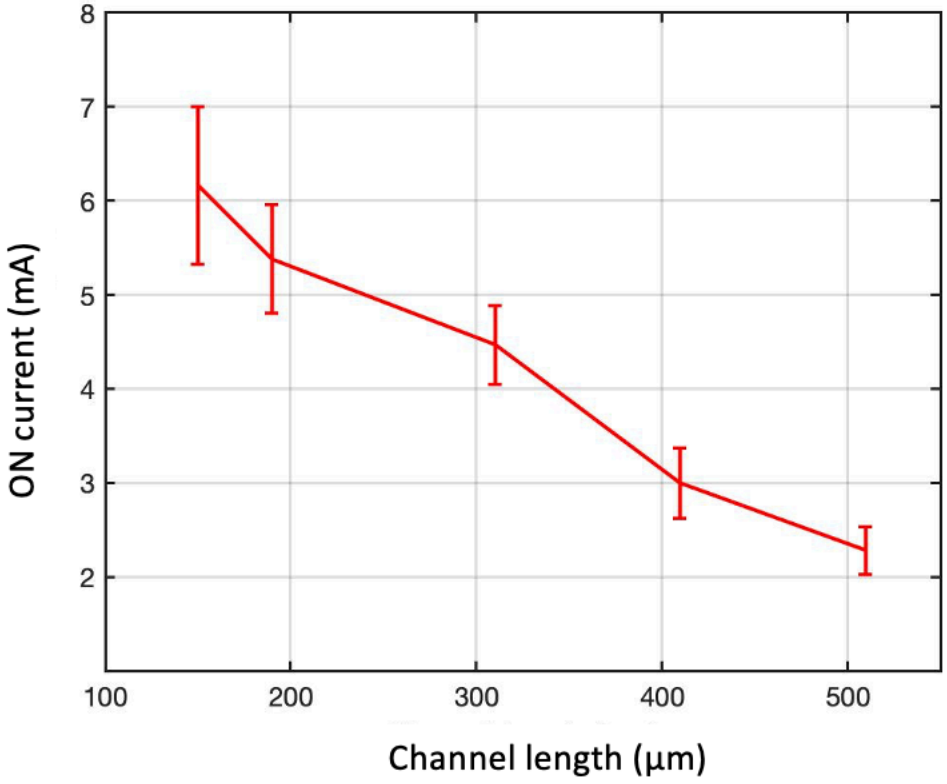

Figure 3-8. Effect of channel length on ON current. ON current is inversely proportional to the channel length.

An OECT can be thought of as a channel resistor (R_{CH}) in series with the source and drain resistors (R_S and R_d) outlined in Equation (3-1) according to the transmission-line method (TLM).

$$R_{tot} = \frac{\partial V_d}{\partial I_d} = R_{CH} + R_S + R_d \tag{3-1}$$

Figure **3-9** (a) displays the total resistance R_{tot} as a function of channel length for various gate voltages and calculated from the linear regime of the I_d-V_d characteristics. The resistance changes linearly with channel length, with slope proportional to channel resistance (RCH). The total resistance for each channel length is shown in **Error! Reference source not found.**. The contact resistance, or R_C, can then be calculated by extrapolating the lines to a channel length of zero. For this experiment, various channel lengths were employed. The contact resistance for different gate voltages is shown in Figure **3-9** (b), which shows that R_C is highly dependent on V_g. Although there are not many reports about the contact resistance of OECTs, low R_C values are obtained at different gate voltages in this work.

Paterson and coworkers [88] investigated modified electrodes and their impact on contact resistance in n-type OECTS. Gold electrodes were fabricated using a lift-off process with OECT channel width of 100 μm. It demonstrates that modifying the gold electrodes with thiol-based self-assembled monolayers (SAMs), 4-methylbenzenethiol (MBT) and pentafluorobenzenethiol (PFBT) is helpful for reducing the contact resistance. However, the lowest contact resistance achieved for V_g= 0.5V was more than 1000 Ωcm, while in this thesis, the contact resistance of 92.48 Ωcm is obtained for V_g= -0.5V.

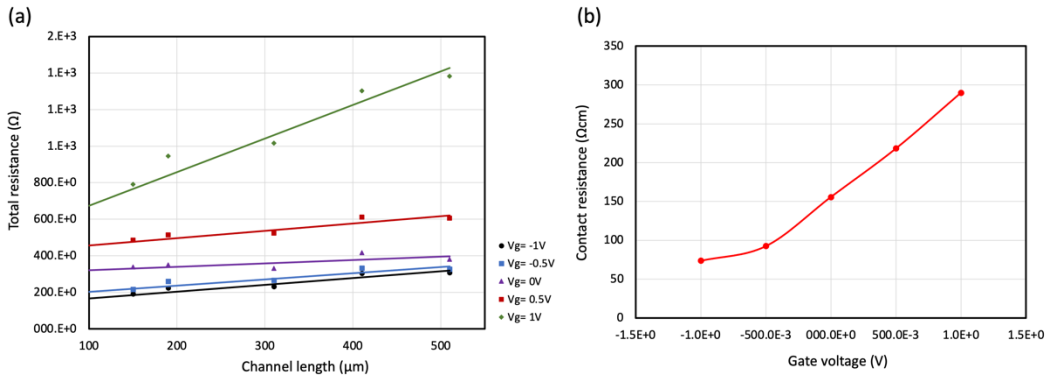

Figure 3-9. (a) The effect of channel length on total resistance of OECTs with various gate voltages. (b) Contact resistance with respect to the gate voltage.

3.4. Time response of LIG based OECT

The drain current versus time was monitored to examine the time responsiveness of LIG-based OECT. According to Figure 3-10, there is a steady state in drain current for the first few seconds when the gate voltage is not applied. The drain current is greatly decreased when a positive gate voltage of +0.5V is supplied, as expected. The rate at which electrolyte ions diffuse into the semiconductor channel determines how long it takes for the drain current to grow. This rising characteristic of the drain current becomes saturated during the period of time after applying voltage to the gate.

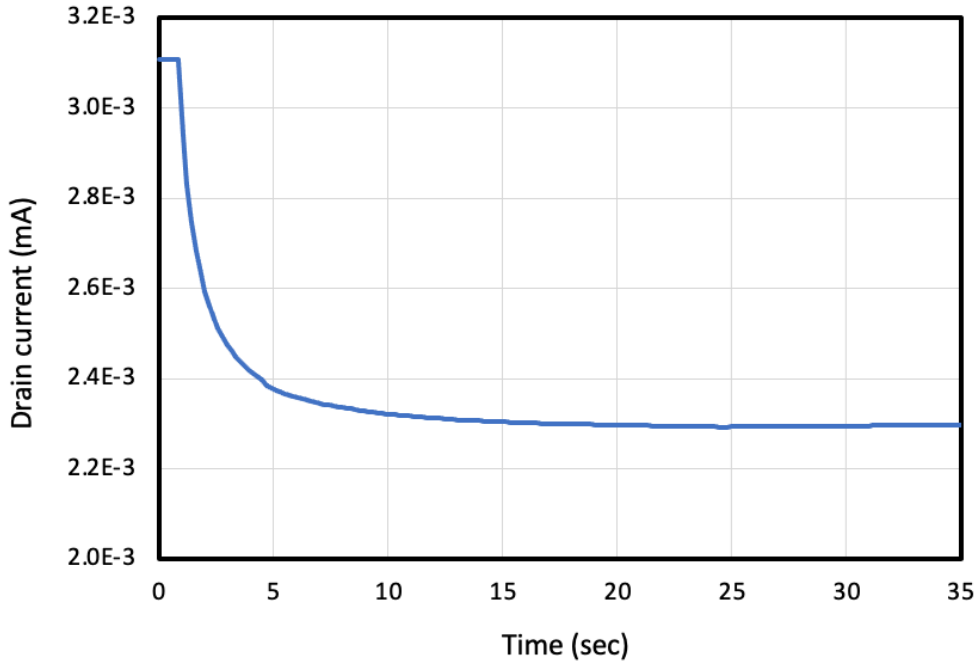

Figure 3-10. Id-t curve for Vg= +0.5 V representing the role of ions in OECTs.

3.5. Effect of sheet resistance on OECT performance

Different laser power and feed rates were used to create the electrodes (gate, source, and drain) to study how well the device performs. Figure **3-11** displays how sheet resistance of different power and feed rate affect OFF and ON currents. It is shown that the tested parameters had not much impact. It is demonstrated that for the gate electrode, OFF and ON currents follow each other in the majority of sheet resistance, even though a precise trend for the functioning of the transistors cannot be determined.

This result is also confirmed in the case of the source and drain electrodes, where the ON-current exhibits the same pattern as the OFF-current. It appears that the performance of the transistors is not much affected by power as a parameter (Figure **3-12**).

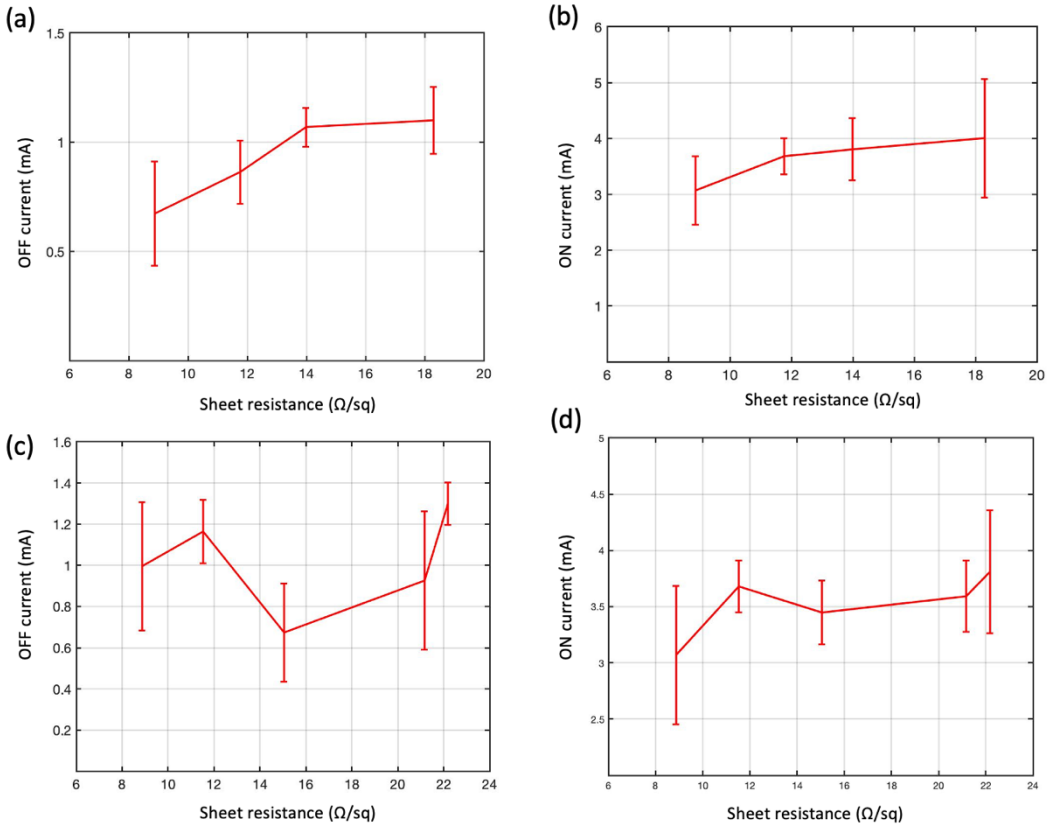

Figure 3-11. Effect of sheet resistance of different feed rate for gate electrode on (a) OFF and (b) ON current. Effect of sheet resistance of different power for gate electrode on (a) OFF and (b) ON current. The feed rate of 500 $mm.min^{-1}$ and power of 35 % are held constant.

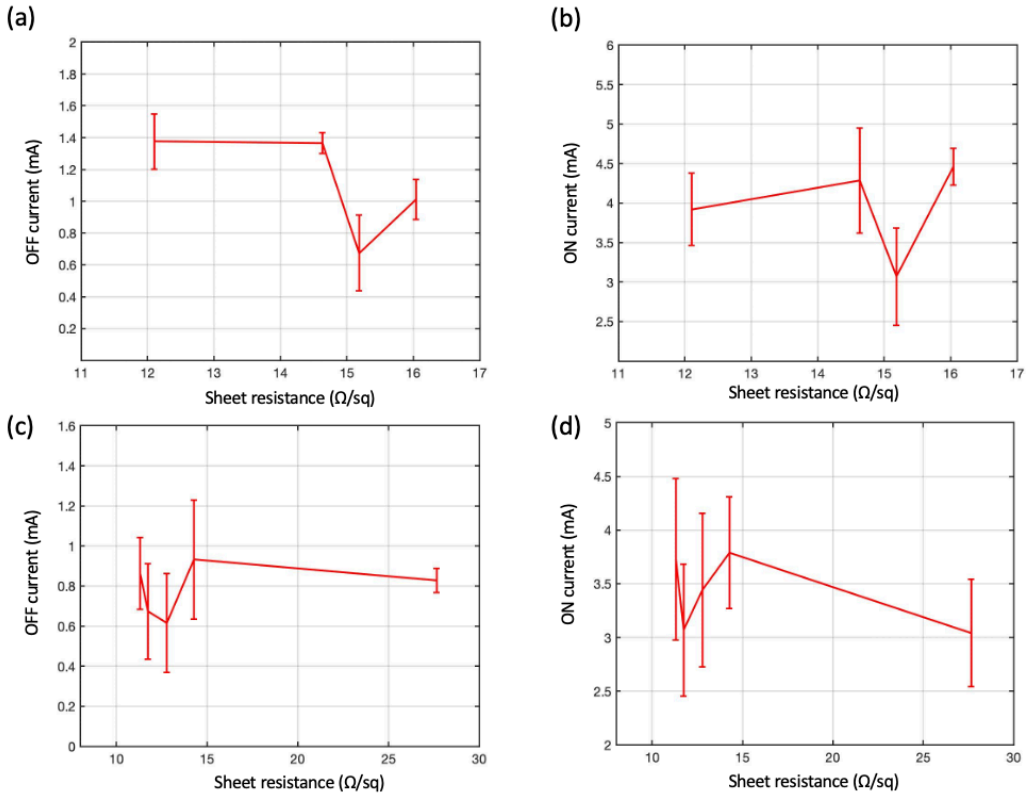

Figure 3-12. Effect of sheet resistance of different feed rate for source and drain electrodes on (a) OFF and (b) ON current. Effect of sheet resistance of different power for source and drain electrodes on (a) OFF and (b) ON current. The feed rate of 1000 mm.min^{-1} and power of 35 % are held constant.

For the LIG-based OECTs demonstrated in this thesis, the source, drain, and gate electrodes can be fabricated in a few minutes and the fabrication process is considerably simpler than other methods. Moreover, as shown in Table 3-2, LIG-based devices exhibit similar or better performance in comparison with many of the reports discussing the metal electrodes on plastic substrates in terms of OFF current,

ON current, and g_m. Also, by comparing the fabrication method of these LIG electrodes with other types of techniques, a limitation is resolution that should be taken into consideration. As shown in Table 3-2, by comparing this work to some methods used for fabrication of metal electrodes, we were able to get a smaller channel length by lasering process. However, the laser spot size is a limitation for getting lower feature size which could potentially be improved in the future. Despite having this limitation to further reduce the channel length, better characteristics are achieved shown in the Table 3-2 which adds to the advantages of these LIG-based OECTs. **Error! Reference source not found.**

Table 3-2. Comparison of OECTs characteristics with literature.

Electrode Material	Electrode Fabrication	Substrate	Channel Material	Channel Fabrication	Gate Material	W (μm)	L (μm)	I_{ON} (mA)	I_{OFF} (mA)	gm (mS)	Voltages (V)	Ref
Au	e-beam evaporator	Si	PEDOT: PSS	Spin coating	PEDOT:PSS-Ag/AgCl	5	10	0.45	0.05	0.98	V_d= -0.6V / V_g= 0.6 to 0V	[62]
Au	e-beam evaporator	Si	PEDOT: PSS	Spin coating	MLG	-	-	-	-	-	V_d= -0.25V / V_g= 1 to -0.5V	[85]
Au	Lift-off Process	Glass	PEDOT: PSS	Spin coating	Au	5	5	2.2	-	2.4	V_d= -0.6V / V_g= 0.8 to 0V	[55]
Au	Lift-off Process	Si	PEDOT: PSS	Spin coating	Si	20	20	4	0.5	1.2	V_d= -0.6V / V_g= 5 to 0V	[89]
Au	e-beam evaporator	PEN	PEDOT: PSS	Spin coating	Nafion/ rGo/CSF	6000	200	4.2	0.2	-	V_d= -0.1V / V_g= 2 to 0V	[90]
Ag	Inkjet Printing	PI	PEDOT: PSS	Spin coating	Graphene	3000	1000	0.195	0.14	0.14	V_d= -0.4V / V_g= 1.6 to 0V	[86]
Ag	Inkjet Printing	PI	PEDOT: PSS	Inkjet printing	Ag	3000	1000	0.46	0.02	1.2	V_d= -0.4V / V_g= 1.6 to 0V	[86]
FTO	Chemical Etching	FTO	PEDOT: PSS	Spin coating	FTO	-	-	0.25	0.025	0.177	V_d= -0.6V / V_g= 2.5 to 0V	[91]
c-PLA	3D Printing	TPC	PEDOT: PSS	Inkjet printing	Ag/AgCl	10000	3000	0.125	0.05	0.25	V_d= -0.6V / V_g= 0.6 to 0V	[67]
LIG	Laser Process	PI	PEDOT: PSS	Inkjet printing	LIG	5000	190	2.564	0.035	2.2	V_d= -1V / V_g= 1 to -1V	This work

3.6. Conclusion

In this chapter, we have shown how to make OECTs using LIG electrodes. These LIG electrodes are created using a CO_2 laser on a PI substrate. It has been shown that the tested laser parameters including different laser power and feed rates had not much impact on device performance. With plasma treatment of the gate electrode, a significant low OFF current was achieved in the reported OECT. The LIG surface area that was exposed to the electrolyte that was placed on top increased thanks to the plasma treatment. High ON-current and ON-OFF ratios are seen in LIG OECTs, which are consistent with the literature. The LIG electrodes were used to accomplish these characteristics.

Chapter 4 . LASER INDUCED GRAPHENE ON 3D PRINTED POLYSULFONE SUBSTRATE

4.1. Introduction

The advantages of 3D printing such as minimal material waste and direct transition to a final product without subtractive procedures led to the use of this technology in a variety of industries, including aerospace, construction, and medical devices. In recent years, 3D printing of electronics has attracted increasing interest due to its potential to provide special features not possible with conventional manufacturing techniques, such as simplified fabrication processes, increased design freedom, novel form factors, decreased weight, and lower prototyping and fabrication costs.

For this application, a variety of alternative carbon-based filaments have been investigated. Even though this filament is very conductive, making graphene and the filament itself is a difficult procedure that is expensive. It has recently been possible to create conductors that convert a polymer substrate into LIG using a straightforward one-step laser-based technique.

Even though LIG on PI and other polymers has been reported on numerous applications, they all use flat substrates. There are three reports that have studied LIG on 3D printed substrate including ULTEM 9085 [75], PEEK [76], and PEI [74]. The LIG's antibacterial, flexibility, and adsorbent qualities have recently been

demonstrated. As a result, it would be beneficial if LIG could be made from the aromatic polysulfone-class of polymers, such as polysulfone (PSU), poly(ether sulfone) (PES), and polyphenylsulfone (PPSU), since these derivatives are widely used polymers in membrane filtration, microelectronic devices, thin film technologies, fuel cells, and biomaterials due to their excellent chemical, thermal, and mechanical properties such as tensile and flexural strength. Also, it has high Young's modulus of 2.48 GPa. Here, in this chapter, we show two important applications of LIG made on 3D printed polysulfone including OECTs and strain gauge.

4.2. Experimental

4.2.1. 3D printing of polysulfone filament

CAD software was used to design the 3D-printed substrates (SolidWorks). The PSU filament was used as the material for an FDM 3D print on a printer (Hydra 16A) from Hyrel 3D (Atlanta, GA). The PSU substrate was fabricated by the high-temperature nozzle, HT1-450. For making LIG OECT on 3D printed PSU substrate, 2.5×2.5 mm^2 square was printed. Also, for the purpose of strain sensor gauge for mechanical test, PSU substrate was created in a dogbone shape. The details of the dogbone dimensions according to the standard test method (ASTM D638-14) are given in Figure 4-1.

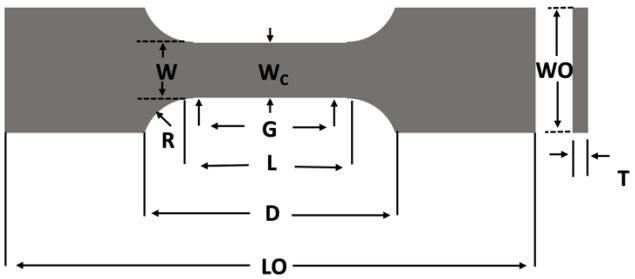

Width of narrow section (W)	3.18 mm
Length of narrow section (L)	9.53 mm
Width overall (WO)	9.53 mm
Length overall (LO)	63.5 mm
Gage length	7.62 mm
Distance between grips (D)	25.4 mm
Radius of fillet (R)	12.7 mm
Thickness (T)	3.2 mm

Figure 4-1. Standard test method for tensile properties of PSU in a dogbone shape. Type V from ASTM D638-14 was chosen for PSU [92].

PSU was printed at nozzle temperature of 380°C, and the temperature of the bed was 170°C. The main printing parameters are listed in Table 4-1.

Table 4-1. Printing parameters of PSU.

Top/bottom pattern	Zig Zag
Line width	0.4 mm
Wall thickness	1 mm
Line height	0.2 mm
Infill pattern	Zig Zag
Infill density	100%
Printing temperature	380 °C
Bed temperature	170 °C
Print speed	40 mm/s
Ironing pattern	Zig Zag
Ironing flow	180 %
Ironing speed	60 mm/s

4.2.2. LIG on 3D printed PSU

The laser procedure was run with a peak power of 40 W. The laser beam had a wavelength of 10.6 μm, a laser spot of 400 μm, and a focal distance of 8 mm. Pulse spacing changes from 500 to 3000 dots per inch (DPI) across all investigations, the distance between the laser head and the substrate (Z) alters from 8 to 25 mm, the laser power varies between 28% and 40% by pulse width modulation, and the scan rate ranges between 300 and 1500 $mm.min^{-1}$. All the laser studies were carried out in ambient condition. The sheet resistance for rectangular patterns was measured using a four-point probe resistivity measuring equipment (Pro4, Signatone, Gilory, CA), and the sheet resistance for line patterns was measured using a probe station with a semiconductor parameter analyzer (Keithley 4200A). The morphology and effects of laser settings on the porosity of lasered patterns were investigated using a field emission scanning electron microscope (FE-SEM) (Thermofisher Quanta 3D). The Raman spectrum was recorded using a Horiba Scientific (LabRAM ARAMIS) Raman microscope with a 532 nm laser with a laser power of 50 mW.

The laser process was used to laser scribe 5 mm long lines and 2.5 mm by 2.5 mm square shapes on polymer sheets. As shown in Figure **4-2**, the vector and nested design of lasering patterns were used to fabricate the LIG electrodes of OECTs on 3D printed PSU substrate. The nested pattern was used for lasering the strain gauge on 3D printed dogbone PSU.

The OECT semiconductor channel and electrolyte are fabricated as described in 3.2.

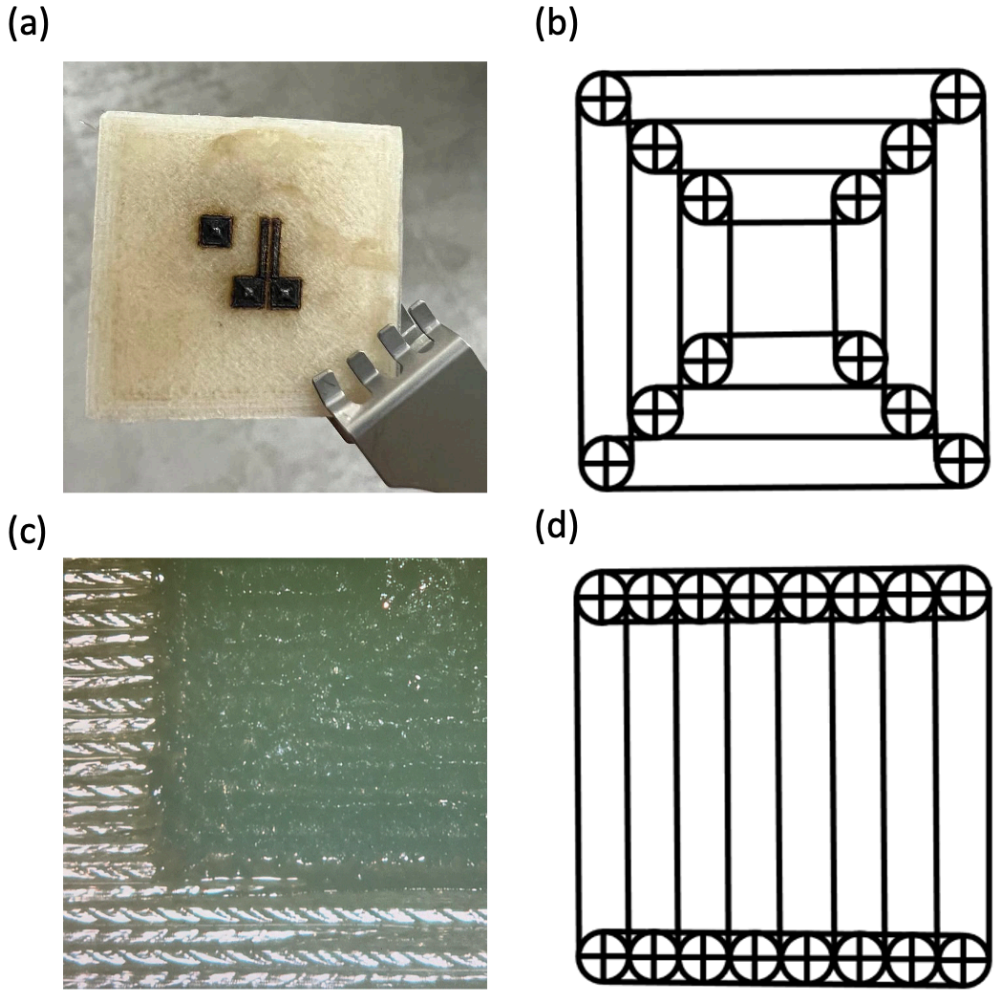

Figure 4-2. (a) LIG based OECT on 3D printed PSU substrate. (b) The nested pattern design used in making LIG OECT on PSU (c) Microscope image of LIG squares. (d) The vector pattern used for fabricating LIG.

4.3. Effect of laser parameters on sheet resistance

In this project, the impact of different laser parameters including power, feed rate, DPI, and Z-position on sheet resistance of LIG squares with vector design was investigated. We prepared four equal LIG square samples for each parameter as shown in Figure 4-3.

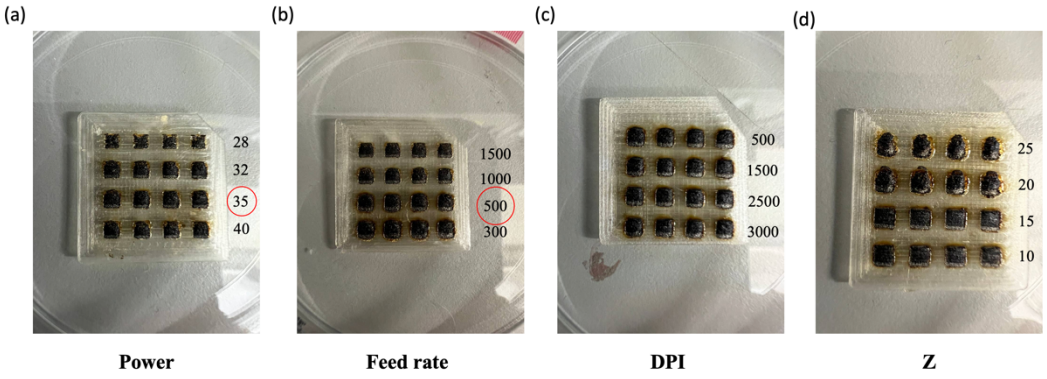

Figure 4-3. (a) samples with different power. Feed rate of 1000 mm.min^{-1}, Z 18 mm, and DPI 2000 are held constant. (b) samples with different feed rate and constant power of 35%, Z 18mm, and DPI of 2000. (c) changing DPI with constant power of 35%, Z of 18 mm, and feed rate of 500 mm.min^{-1}. (d) samples with various Z-positions and constant power of 35%, DPI of 2000, and feed rate of 500 mm.min^{-1}.

Figure 4-4 shows the effect of different parameters on sheet resistance for LIG made on PSU substrate. For each laser parameter in this experiment, four samples were used for measuring the sheet resistance. Figure 4-4 (a) illustrates that lower sheet resistance can be achieved at power of 35%. The lower and higher power led to the

higher sheet resistance. In terms of height (Z), Figure 4-4 (b) demonstrates that increasing Z causes higher sheet resistance since the power density is lower for the laser beam reaching the PSU substrate. The lowest sheet resistance of 2.72 Ω/sq was achieved at height of 10 mm. The lower height at 9 mm was also investigated in this experiment which showed burning and no LIG line was formed. Effect of feed rate is investigated in Figure 4-4 (c) in which increasing the feed rate results in higher sheet resistance. According to Figure 4-4 (d), although DPI of 1500 had a lower sheet resistance than the others, there is still no significant difference between various DPI.

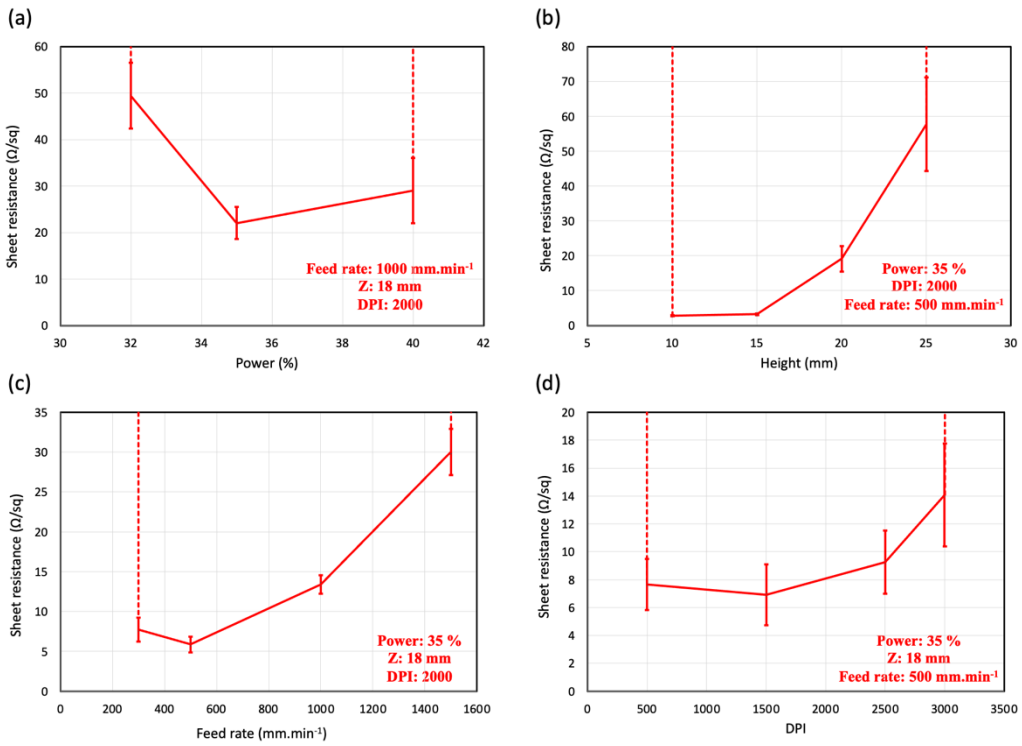

Figure 4-4. Effect of (a) power, (b) height, (c) feed rate, and (d) DPI on sheet resistance.

4.4. Investigation of LIG morphology lasered on 3D printed polysulfone

The morphology of LIG on 3D printed PSU at various laser powers is shown in Figure 4-5. The laser passes are more disorganized when the power is increased from 28% to 40%. The spherical morphology is the dominant part of the LIG morphology fabricated on 3D printed polysulfone. It seems that the polysulfone substrate helps LIG to grow with a fibrous morphology. By increasing the power from 28% to 40%, more mixed (spherical and fibrous) morphology can be seen. In terms of feed rate, it is clearly shown in Figure 4-6 that by increasing the feed rate from 500 to 1500 $mm.min^{-1}$, the more fibrous morphology is achieved.

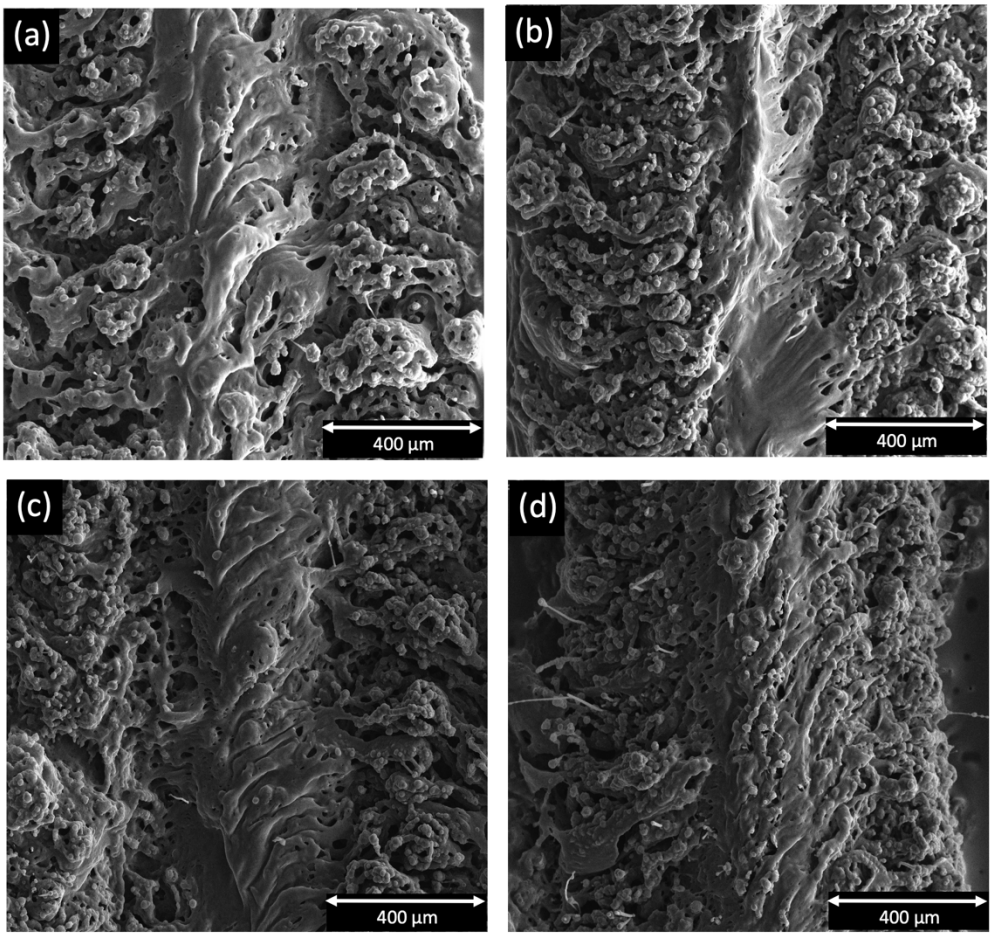

Figure 4-5. SEM images of LIG made on 3D printed PSU with power of (a) 28, (b) 35, (c) 38, and (d) 40%. Feed rate of 500 mm.min^{-1} is held constant.

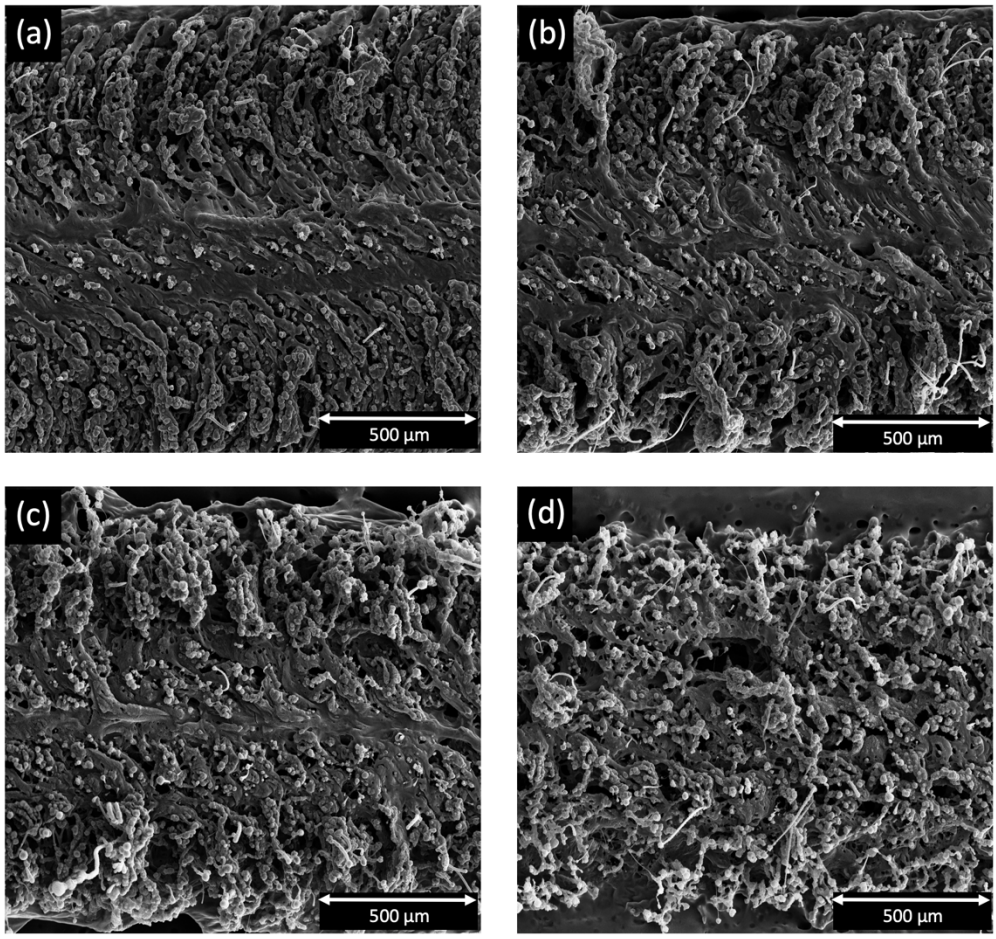

Figure 4-6. SEM images of LIG made on 3D printed PSU with power of (a) 500, (b) 800, (c)1000, and (d) 1500 mm.min^{-1}. Power of 35% is held constant.

4.5. Raman Spectroscopy

In Figure 4-7 (a), the Raman spectrum is shown for the PSU substrate. To prove LIG fabrication after lasering the 3D printed PSU substrate, Raman spectroscopy was measured for LIG with feed rate of 500 mm.min^{-1} and power of 35% as shown in Figure 4-7 (b). The existence of graphene's unique peaks confirms its presence. Wavenumbers of 1350, 1550, and 2700 cm^{-1}, respectively, correspond to the D, G, and 2D peaks, which signify the presence of multi-layer graphene. The sample's 2D peak is only a broad peak with a moderate intensity. High-temperature annealed nano graphite is the linking peak formed by the interconnecting D and G bands.

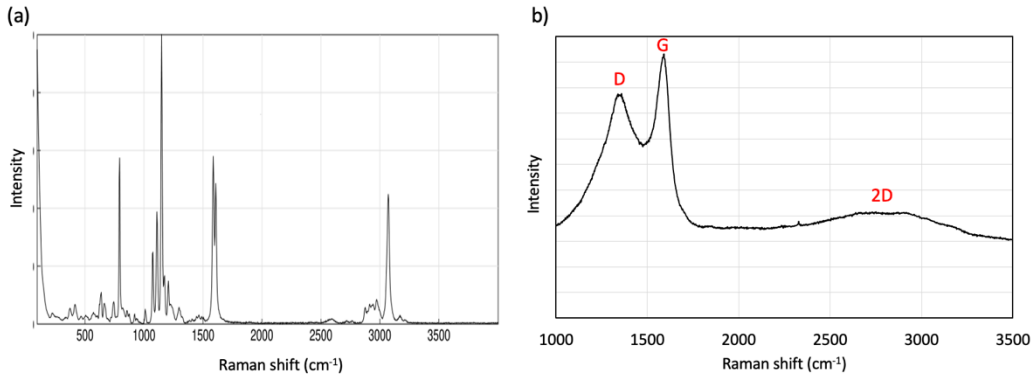

Figure 4-7. Raman spectra of (a) PSU substrate and (b) LIG made on 3D printed PSU substrate. Power of 35% and feed rate of 500 mm.min^{-1} was used.

4.6. Applications

4.6.1. OECTs

Figure 4-8 (a) depicts a transfer curve for the LIG-based OECT in the saturation regime. For source, drain, and gate electrodes, laser parameters were fixed at a power of 35% and a feed rate of 500 $mm.min^{-1}$. As seen in Figure 4-8 (a), with a constant V_d= -1V, the drain current amplitude decreases as V_g grows more positive. In the double sweep observations, the slow ion migration causes a small hysteresis. The OFF current is 0.151 mA. For the given device, the ON current and ON-OFF ratio are 1.3276 mA and 8.768, respectively.

Figure 4-8 (b) displays the output characteristics. At low drain voltages, the channel current shows a linear relationship with V_d, but at higher V_d values, it does not reach full saturation.

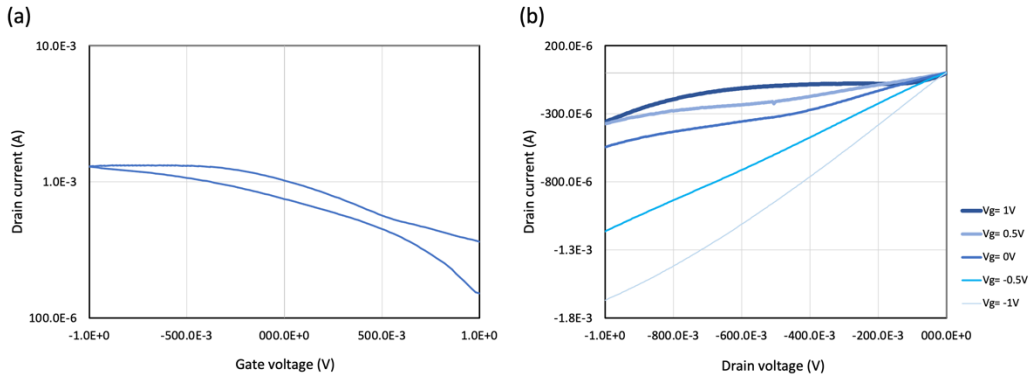

Figure 4-8. a) Transfer and (b) output curves of LIG-based OECTs fabricated on 3D printed PSU.

4.6.2. Strain gauge

A strain gauge is engraved with power of 35% and feed rate of 1500 $mm.min^{-1}$ on a 3D printed substrate to test the produced conductors in an application. The nested pattern was used to fabricate LIG on a dogbone shape for using in mechanical test. On each substrate, the manufactured strain gauge is depicted in Figure 4-9. The strain gauge on the 3D printed PSU has a starting resistance of 136 Ω.

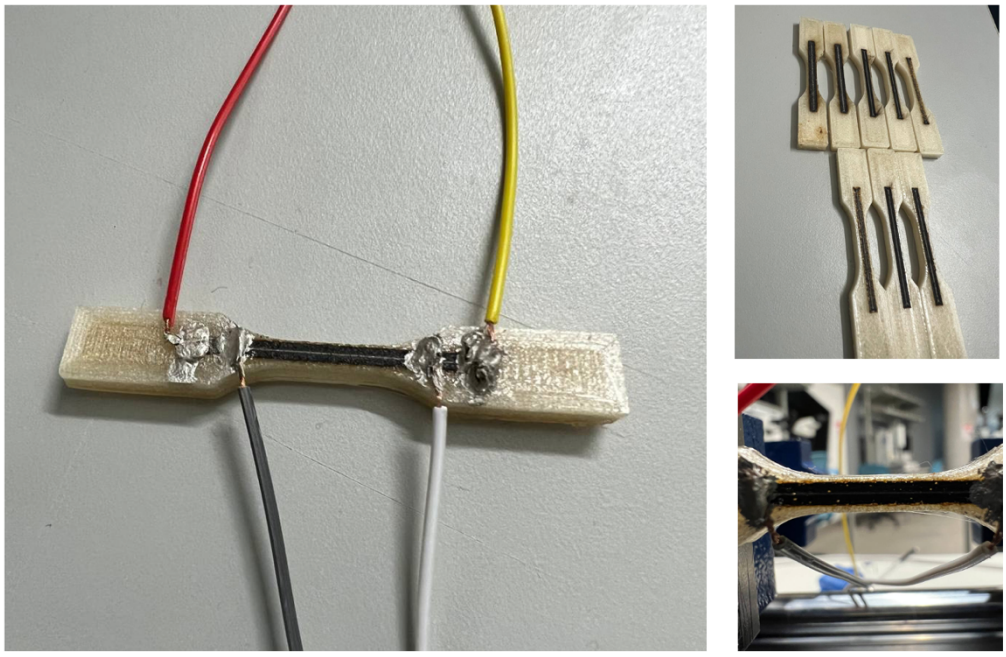

Figure 4-9. Strain gauge engraved on 3D printed PSU.

A picture of the tensile test setup used to test the manufactured strain sensors in the tensile mode is shown in Figure 4-10 (a). To measure the resistance as a function of applied strain, the silver paste connection pads on each sample are linked to a semiconductor parameter analyzer (Keithley 4200A) as shown in Figure 4-10 (c). Figure 4-10 (b) depicts the resistance variation as a function of time. The speed was 200 μm/s, max force was 600 N, and the sensing interval was 20 μm. The resistance exhibits high stability throughout this procedure. It shows that the sensors are stable even under significant deformations. For motion capture, it's also crucial to have a quick response time and less hysteresis.

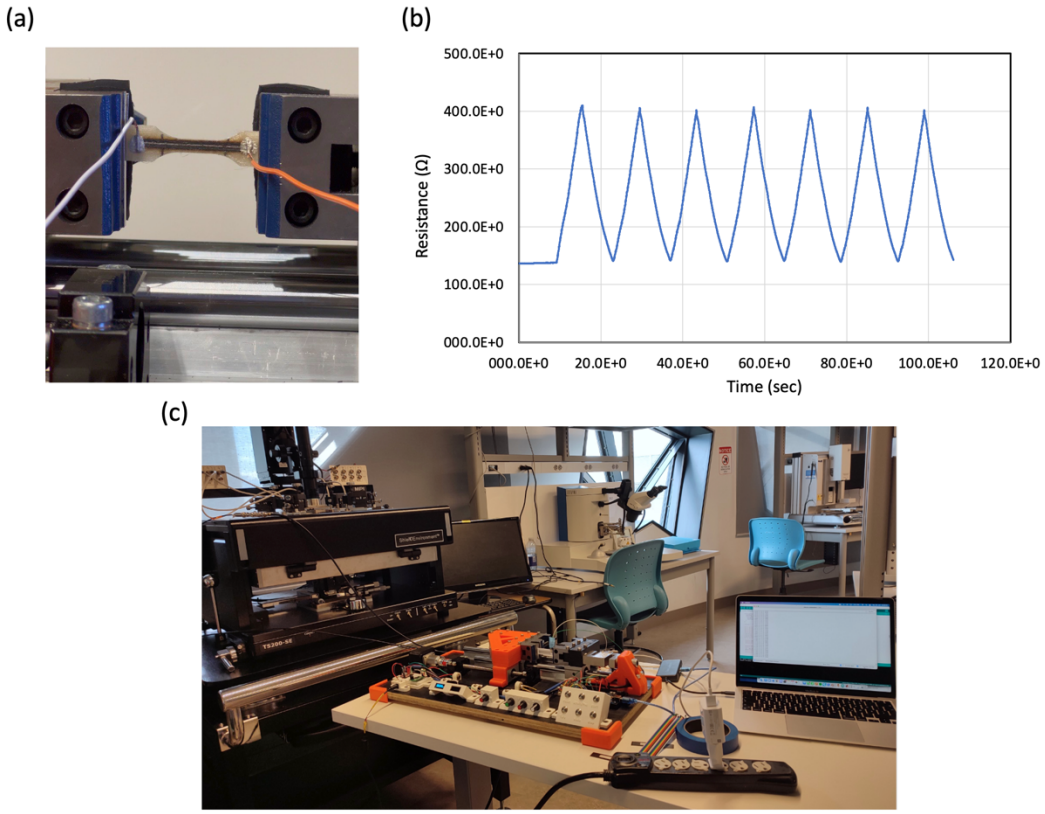

Figure 4-10. (a) Tensile test setup for LIG mechanical strain sensors on 3D printed PSU. (b) The resistance versus time for several expansion and shrinkage. (c) Tensile test machine connecting to the probe station.

One of the main factors for sensors is sensitivity which is represented by the gauge factor (GF). GF is calculated using Equation (**4-1**), where ΔR stands for resistance changes, R0 for initial resistance, and ε for strain. The results obtained through Equation (**4-1**) are represented on Figure 4-11 (a). The strain calculated by measuring the markers' movements using ImageJ software is 0.02. Resistance

change was 976 Ω which results in the remarkable gauge factor of around 300. The resistance changes versus applied stress on the strain gauge is shown in Figure **4-11** (b). The high sensitivity is expected from this sensor since there are several stages. First, the small stress can cause the slippage of the LIG sheets that increases the resistance gradually. Microcracks are created as stress is raised further. This can cause the severance of conductive pathways which increases the resistance dramatically. The sensor is most sensitive to further deformation in the final stage, when the stress approaches the higher values, because the regular cracks drastically reduce the conductive routes.

$$GF = \frac{\frac{\Delta R}{R0}}{\varepsilon} \tag{4-1}$$

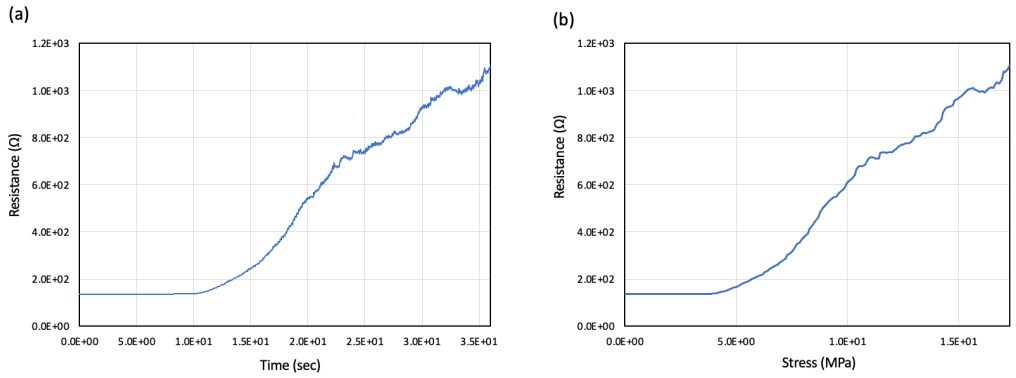

Figure 4-11. (a) Resistance changes when strain is applied to the engraved strain gauge on the 3D printed PSU. (b) Resistance changes after applying stress to the LIG-based strain gauge on 3D printed PSU.

4.7. Conclusion

We have used a CO_2 laser to show how a 3D printed polymer (PSU) can be directly transformed into graphene. The best results of 2.72 Ω/sq for sheet resistance were achieved by adjusting the laser power, feed rate, height, and DPI. In this thesis, LIG on 3D printed PSU was used in two different applications. LIG source, drain, and gate electrodes were used in OECTs. The OFF current is 0.151 mA. The ON current for the specified device is 1.3276 mA, and the ON-OFF ratio is 8.768, correspondingly. Also, due to the remarkable mechanical properties of PSU and the flexibility of LIG, LIG was used as a strain gauge for the mechanical tests. The sensor demonstrated very good stability, and also the remarkable gauge factor of 300 was achieved.

Chapter 5 . CONCLUSION AND FUTURE WORK

The findings from this research are detailed in this chapter. After that, ideas are offered for more research that could expand on this thesis' findings.

5.1. Conclusions

Graphene-based devices are created on several polymeric substrates in this thesis using inexpensive techniques. Flexibility and excellent conductivity are provided by the incorporation of graphene with 3D printed structures using LIG and inkjet printing processes. Additionally, the versatility of LIG designs allows for a wide range of applications. Different sensing applications such as mechanical sensors and OECTs are made possible by the combination of laser-induced graphene (LIG), 3D printing, and inkjet printing.

In Chapter 2, a CO_2 laser is used to convert polyimide (PI) into graphene. In order to improve the resulting sheet resistance of LIG, various parameters are looked into. The laser process used to create the square-patterned electrodes yielded a minimum sheet resistance of 7.86 Ω/sq. The material characterizations demonstrate that the produced graphene on PI substrate has porosity which varies by different laser parameters. Also, Raman spectroscopy confirms that LIG is produced by lasering the PI tape with the mentioned laser parameters.

In Chapter 3, LIG is used as source, drain, and gate electrodes in a co-planar architecture used in organic electrochemical transistors (OECT). P-type semiconductor PEDOT:PSS is inkjet-printed between source and drain electrode as the channel of transistor. I-V curves are used to extract various characteristics like I_{ON}/I_{OFF}, V_{th}, and transconductance (gm) to observe the impact of different conditions. The results show that devices with the plasma treated gate electrode demonstrates very low OFF current and high ON-OFF ratio of 72.80. Additionally, short channel devices have been shown to perform better.

In Chapter 4, LIG is engraved on 3D printed polysulfone (PSU) polymeric substrate via CO_2 laser for the first time. It has been shown that different laser parameters such as power, feed rate, DPI, and height can affect the sheet resistance of LIG. At a height of 10 mm, the lowest sheet resistance of 2.72 /sq was obtained. For the purpose of electronics integration on various 3D printed geometries and architectures, LIG-based devices are shown. One main application shown in this chapter was OECTs, which exhibit OFF current of 0.151 mA, ON current of 1.3276 mA, ON-OFF ratio of 8.768. Also, due to the remarkable mechanical properties of PSU, LIG has been shown as a strain gauge on 3D printed dogbone shape of PSU. Remarkable sensitivity of 300 is achieved via this strain sensor.

5.2. Future work

LIG-based OECTs are fabricated for the first time. Various electrodes architecture can be used to improve the performance of this device in terms of OFF and ON current and gm. Different parts of the electrodes can be plasma treated which might be helpful in optimizing the performance of the device. Using two gates might be effective in maximizing the voltage drop in the semiconductor-electrolyte interface. Also, NaCl is reported as an electrolyte in this thesis which is deposited via drop casting method. There are electrolytes with higher viscosity that could be printed as an electrolyte on top of the transistor's channel and gate electrode which help the device to be more stable on the ambient condition.

In the PEDOT:PSS inkjet printing process, there could be some optimization in ink formulation, which can help the doping process occurred in the semiconductor channel. This can change the ion movements and helpful to get a better device. Using some de-dopant in ink formulation could be helpful in making the better devices.

There are many applications for the generated laser-induced graphene on 3D printed PSU due to its low sheet resistance. A strain sensor setup can be used to test the intended strain gauges. This method of fabricating strain sensors enables the testing of various strain gauge pattern designs. Graphene conductors may be used to create

a variety of complicated 3D structures because the substrate is made using 3D printing.

Chapter 6 . REFERENCES

[1] G. Yang, L. Li, W. B. Lee, and M. C. Ng, "Structure of graphene and its disorders: a review," *Sci. Technol. Adv. Mater.*, vol. 19, no. 1, pp. 613–648, Dec. 2018, doi: 10.1080/14686996.2018.1494493.

[2] M. Engel *et al.*, "Graphene-enabled and directed nanomaterial placement from solution for large-scale device integration," *Nat. Commun.*, vol. 9, no. 1, p. 4095, Dec. 2018, doi: 10.1038/s41467-018-06604-4.

[3] S. H. Chae and Y. H. Lee, "Carbon nanotubes and graphene towards soft electronics," *Nano Converg.*, vol. 1, no. 1, p. 15, Dec. 2014, doi: 10.1186/s40580-014-0015-5.

[4] M. Fedel, "Hemocompatibility of Carbon Nanostructures," *C — J. Carbon Res.*, vol. 6, no. 1, p. 12, Mar. 2020, doi: 10.3390/c6010012.

[5] Z. Zhang *et al.*, "All-carbon sp-sp2 hybrid structures: Geometrical properties, current rectification and current amplification," *Sci. Rep.*, vol. 3, no. 1, p. 2575, Dec. 2013, doi: 10.1038/srep02575.

[6] Md. S. A. Bhuyan, Md. N. Uddin, Md. M. Islam, F. A. Bipasha, and S. S. Hossain, "Synthesis of graphene," *Int. Nano Lett.*, vol. 6, no. 2, pp. 65–83, Jun. 2016, doi: 10.1007/s40089-015-0176-1.

[7] M. S. Yoo *et al.*, "Growth of Multilayer Graphene with a Built-in Vertical Electric Field," *Chem. Mater.*, vol. 32, no. 12, pp. 5142–5152, Jun. 2020, doi: 10.1021/acs.chemmater.0c01145.

[8] Z. Wei, Z. Ni, K. Bi, M. Chen, and Y. Chen, "In-plane lattice thermal conductivities of multilayer graphene films," *Carbon*, vol. 49, no. 8, pp. 2653–2658, Jul. 2011, doi: 10.1016/j.carbon.2011.02.051.

[9] J. H. Gosling *et al.*, "Universal mobility characteristics of graphene originating from charge scattering by ionised impurities," *Commun. Phys.*, vol. 4, no. 1, p. 30, Feb. 2021, doi: 10.1038/s42005-021-00518-2.

[10] T. S. Sreeprasad and V. Berry, "How Do the Electrical Properties of Graphene Change with its Functionalization?," *Small*, vol. 9, no. 3, pp. 341–350, Feb. 2013, doi: 10.1002/smll.201202196.

[11] Z. H. Khan, A. R. Kermany, A. Öchsner, and F. Iacopi, "Mechanical and electromechanical properties of graphene and their potential application in MEMS," *J. Phys. Appl. Phys.*, vol. 50, no. 5, p. 053003, Feb. 2017, doi: 10.1088/1361-6463/50/5/053003.

[12] W. Choi, I. Lahiri, R. Seelaboyina, and Y. S. Kang, "Synthesis of Graphene and Its Applications: A Review," *Crit. Rev. Solid State Mater. Sci.*, vol. 35, no. 1, pp. 52–71, Feb. 2010, doi: 10.1080/10408430903505036.

[13] H. Murata, Y. Nakajima, N. Saitoh, N. Yoshizawa, T. Suemasu, and K. Toko, “High-Electrical-Conductivity Multilayer Graphene Formed by Layer Exchange with Controlled Thickness and Interlayer,” *Sci. Rep.*, vol. 9, no. 1, p. 4068, Dec. 2019, doi: 10.1038/s41598-019-40547-0.

[14] A. A. Balandin *et al.*, “Superior Thermal Conductivity of Single-Layer Graphene,” *Nano Lett.*, vol. 8, no. 3, pp. 902–907, Mar. 2008, doi: 10.1021/nl0731872.

[15] A. Ghosh *et al.*, “Uptake of H $_2$ and CO $_2$ by Graphene,” *J. Phys. Chem. C*, vol. 112, no. 40, pp. 15704–15707, Oct. 2008, doi: 10.1021/jp805802w.

[16] D. G. Papageorgiou, I. A. Kinloch, and R. J. Young, “Mechanical properties of graphene and graphene-based nanocomposites,” *Prog. Mater. Sci.*, vol. 90, pp. 75–127, Oct. 2017, doi: 10.1016/j.pmatsci.2017.07.004.

[17] L. Lin, H. Peng, and Z. Liu, “Synthesis challenges for graphene industry,” *Nat. Mater.*, vol. 18, no. 6, pp. 520–524, Jun. 2019, doi: 10.1038/s41563-019-0341-4.

[18] N. Kumar *et al.*, “Top-down synthesis of graphene: A comprehensive review,” *FlatChem*, vol. 27, p. 100224, May 2021, doi: 10.1016/j.flatc.2021.100224.

[19] D. M. P. Ghatule and U. A. Devare, “Study and Analysis on Synthesis of Graphene and its Applications in Solar Cells,” *Int. J. Innov. Resear Ch Adv. Eng. Ing*, vol. 2, no. 1, p. 3, 2015.

[20] A. Pirzado *et al.*, “Few-Layer Graphene from Mechanical Exfoliation of Graphite-Based Materials: Structure-Dependent Characteristics,” *ChemEngineering*, vol. 3, no. 2, p. 37, Apr. 2019, doi: 10.3390/chemengineering3020037.

[21] M. Yi and Z. Shen, “A review on mechanical exfoliation for the scalable production of graphene,” *J. Mater. Chem. A*, vol. 3, no. 22, pp. 11700–11715, 2015, doi: 10.1039/C5TA00252D.

[22] H. C. Lee *et al.*, “Review of the synthesis, transfer, characterization and growth mechanisms of single and multilayer graphene,” *RSC Adv.*, vol. 7, no. 26, pp. 15644–15693, 2017, doi: 10.1039/C7RA00392G.

[23] M. Saeed, Y. Alshammari, S. A. Majeed, and E. Al-Nasrallah, “Chemical Vapour Deposition of Graphene—Synthesis, Characterisation, and Applications: A Review,” *Molecules*, vol. 25, no. 17, p. 3856, Aug. 2020, doi: 10.3390/molecules25173856.

[24] Q. Zheng and J.-K. Kim, *Graphene for Transparent Conductors*. New York, NY: Springer New York, 2015. doi: 10.1007/978-1-4939-2769-2.

[25] Y. Song, W. Zou, Q. Lu, L. Lin, and Z. Liu, “Graphene Transfer: Paving the Road for Applications of Chemical Vapor Deposition Graphene,” *Small*, vol. 17, no. 48, p. 2007600, Dec. 2021, doi: 10.1002/smll.202007600.

[26] H. Van Ngoc, Y. Qian, S. K. Han, and D. J. Kang, “PMMA-Etching-Free Transfer of Wafer-scale Chemical Vapor Deposition Two-dimensional Atomic Crystal by a Water Soluble Polyvinyl Alcohol Polymer Method,” *Sci. Rep.*, vol. 6, no. 1, p. 33096, Dec. 2016, doi: 10.1038/srep33096.
[27] Y. Khan, A. Thielens, S. Muin, J. Ting, C. Baumbauer, and A. C. Arias, “A New Frontier of Printed Electronics: Flexible Hybrid Electronics,” *Adv. Mater.*, vol. 32, no. 15, p. 1905279, Apr. 2020, doi: 10.1002/adma.201905279.
[28] M. R. Islam *et al.*, “Fully printed and multifunctional graphene-based wearable e-textiles for personalized healthcare applications,” *iScience*, vol. 25, no. 3, p. 103945, Mar. 2022, doi: 10.1016/j.isci.2022.103945.
[29] T. Pandhi *et al.*, “Fully inkjet-printed multilayered graphene-based flexible electrodes for repeatable electrochemical response,” *RSC Adv.*, vol. 10, no. 63, pp. 38205–38219, 2020, doi: 10.1039/D0RA04786D.
[30] P. He *et al.*, “Screen-Printing of a Highly Conductive Graphene Ink for Flexible Printed Electronics,” *ACS Appl. Mater. Interfaces*, vol. 11, no. 35, pp. 32225–32234, Sep. 2019, doi: 10.1021/acsami.9b04589.
[31] J. Lin *et al.*, “Laser-induced porous graphene films from commercial polymers,” *Nat. Commun.*, vol. 5, no. 1, p. 5714, Dec. 2014, doi: 10.1038/ncomms6714.
[32] R. Srinivasan, R. R. Hall, W. D. Wilson, W. D. Loehle, and D. C. Allbee, “Formation of a Porous, Patternable, Electrically Conducting Carbon Network by the Ultraviolet Laser Irradiation of the Polyimide PMDA-ODA (Kapton),” *Chem. Mater.*, vol. 6, no. 7, pp. 888–889, Jul. 1994, doi: 10.1021/cm00043a005.
[33] Y. Chyan, R. Ye, Y. Li, S. P. Singh, C. J. Arnusch, and J. M. Tour, “Laser-Induced Graphene by Multiple Lasing: Toward Electronics on Cloth, Paper, and Food,” *ACS Nano*, vol. 12, no. 3, pp. 2176–2183, Mar. 2018, doi: 10.1021/acsnano.7b08539.
[34] D. S. Bergsman, B. A. Getachew, C. B. Cooper, and J. C. Grossman, “Preserving nanoscale features in polymers during laser induced graphene formation using sequential infiltration synthesis,” *Nat. Commun.*, vol. 11, no. 1, p. 3636, Dec. 2020, doi: 10.1038/s41467-020-17259-5.
[35] A. K. Thakur, B. Lin, F. H. Nowrin, and M. Malmali, “Comparing Structure and Sorption Characteristics of Laser-Induced Graphene (LIG) from Various Polymeric Substrates,” *ACS EST Water*, vol. 2, no. 1, pp. 75–87, Jan. 2022, doi: 10.1021/acsestwater.1c00259.
[36] K. Sinha, “Laser Induced Graphene on Lignin Upgraded Stretchable Polymer Films,” p. 72.
[37] B. A. Getachew, D. S. Bergsman, and J. C. Grossman, “Laser-Induced Graphene from Polyimide and Polyethersulfone Precursors as a Sensing Electrode in Anodic Stripping Voltammetry,” *ACS Appl. Mater. Interfaces*, vol. 12, no. 43, pp. 48511–48517, Oct. 2020, doi: 10.1021/acsami.0c11725.

[38] A. Minhas-Khan, S. Nambi, and G. Grau, “Low-resistance laser-induced graphitic carbon by maximizing energy delivery and pulse overlap,” *Carbon*, vol. 181, pp. 310–322, Aug. 2021, doi: 10.1016/j.carbon.2021.05.037.
[39] A. Imbrogno *et al.*, “Laser-Induced Graphene Supercapacitors by Direct Laser Writing of Cork Natural Substrates,” *ACS Appl. Electron. Mater.*, vol. 4, no. 4, pp. 1541–1551, Apr. 2022, doi: 10.1021/acsaelm.1c01202.
[40] P. Zaccagnini and A. Lamberti, “A perspective on laser-induced graphene for micro-supercapacitor application,” *Appl. Phys. Lett.*, vol. 120, no. 10, p. 100501, Mar. 2022, doi: 10.1063/5.0078707.
[41] R. K. Mishra, A. Krishnakumar, A. Zareei, U. Heredia-Rivera, and R. Rahimi, “Electrochemical sensor for rapid detection of fentanyl using laser-induced porous carbon-electrodes,” *Microchim. Acta*, vol. 189, no. 5, p. 198, May 2022, doi: 10.1007/s00604-022-05299-1.
[42] J. Yi *et al.*, “Facile Patterning of Laser-Induced Graphene with Tailored Li Nucleation Kinetics for Stable Lithium-Metal Batteries,” *Adv. Energy Mater.*, vol. 9, no. 38, p. 1901796, Oct. 2019, doi: 10.1002/aenm.201901796.
[43] M. Ren *et al.*, “CO $_2$ to Formic Acid Using Cu–Sn on Laser-Induced Graphene,” *ACS Appl. Mater. Interfaces*, vol. 12, no. 37, pp. 41223–41229, Sep. 2020, doi: 10.1021/acsami.0c08964.
[44] M. G. Stanford *et al.*, “Self-Sterilizing Laser-Induced Graphene Bacterial Air Filter,” *ACS Nano*, vol. 13, no. 10, pp. 11912–11920, Oct. 2019, doi: 10.1021/acsnano.9b05983.
[45] N. A. Kyeremateng, T. Brousse, and D. Pech, “Microsupercapacitors as miniaturized energy-storage components for on-chip electronics,” *Nat. Nanotechnol.*, vol. 12, no. 1, pp. 7–15, Jan. 2017, doi: 10.1038/nnano.2016.196.
[46] W. Gao *et al.*, “Direct laser writing of micro-supercapacitors on hydrated graphite oxide films,” *Nat. Nanotechnol.*, vol. 6, no. 8, pp. 496–500, Aug. 2011, doi: 10.1038/nnano.2011.110.
[47] Z. Peng, J. Lin, R. Ye, E. L. G. Samuel, and J. M. Tour, “Flexible and Stackable Laser-Induced Graphene Supercapacitors,” *ACS Appl. Mater. Interfaces*, vol. 7, no. 5, pp. 3414–3419, Feb. 2015, doi: 10.1021/am509065d.
[48] L. Huang *et al.*, “Wearable Flexible Strain Sensor Based on Three-Dimensional Wavy Laser-Induced Graphene and Silicone Rubber,” *Sensors*, vol. 20, no. 15, p. 4266, Jul. 2020, doi: 10.3390/s20154266.
[49] L.-Q. Tao *et al.*, “An intelligent artificial throat with sound-sensing ability based on laser induced graphene,” *Nat. Commun.*, vol. 8, no. 1, p. 14579, Apr. 2017, doi: 10.1038/ncomms14579.
[50] R. M. Torrente-Rodríguez *et al.*, “Investigation of Cortisol Dynamics in Human Sweat Using a Graphene-Based Wireless mHealth System,” *Matter*, vol. 2, no. 4, pp. 921–937, Apr. 2020, doi: 10.1016/j.matt.2020.01.021.

[51] N. Dixit and S. P. Singh, “Laser-Induced Graphene (LIG) as a Smart and Sustainable Material to Restrain Pandemics and Endemics: A Perspective,” *ACS Omega*, vol. 7, no. 6, pp. 5112–5130, Feb. 2022, doi: 10.1021/acsomega.1c06093.

[52] J. T. Friedlein, R. R. McLeod, and J. Rivnay, “Device physics of organic electrochemical transistors,” *Org. Electron.*, vol. 63, pp. 398–414, Dec. 2018, doi: 10.1016/j.orgel.2018.09.010.

[53] D. A. Bernards and G. G. Malliaras, “Steady-State and Transient Behavior of Organic Electrochemical Transistors,” *Adv. Funct. Mater.*, vol. 17, no. 17, pp. 3538–3544, Nov. 2007, doi: 10.1002/adfm.200601239.

[54] S. L. Bidinger, S. Han, G. G. Malliaras, and T. Hasan, “Highly stable PEDOT:PSS electrochemical transistors,” *Appl. Phys. Lett.*, vol. 120, no. 7, p. 073302, Feb. 2022, doi: 10.1063/5.0079011.

[55] F. Hempel *et al.*, “PEDOT:PSS organic electrochemical transistors for electrical cell-substrate impedance sensing down to single cells,” *Biosens. Bioelectron.*, vol. 180, p. 113101, May 2021, doi: 10.1016/j.bios.2021.113101.

[56] J. Rivnay, S. Inal, A. Salleo, R. M. Owens, M. Berggren, and G. G. Malliaras, “Organic electrochemical transistors,” *Nat. Rev. Mater.*, vol. 3, no. 2, p. 17086, Feb. 2018, doi: 10.1038/natrevmats.2017.86.

[57] P. R. Paudel, J. Tropp, V. Kaphle, J. D. Azoulay, and B. Lüssem, “Organic electrochemical transistors – from device models to a targeted design of materials,” *J. Mater. Chem. C*, vol. 9, no. 31, pp. 9761–9790, 2021, doi: 10.1039/D1TC01601F.

[58] J. K. Wassei and R. B. Kaner, “Graphene, a promising transparent conductor,” *Mater. Today*, vol. 13, no. 3, pp. 52–59, Mar. 2010, doi: 10.1016/S1369-7021(10)70034-1.

[59] C. Y. Foo, H. N. Lim, M. A. Mahdi, M. H. Wahid, and N. M. Huang, “Three-Dimensional Printed Electrode and Its Novel Applications in Electronic Devices,” *Sci. Rep.*, vol. 8, no. 1, p. 7399, Dec. 2018, doi: 10.1038/s41598-018-25861-3.

[60] A. Sun *et al.*, “Pd gated AlGaN/GaN high electron mobility transistor for ppb level hydrogen gas detection,” *Int. J. Hydrog. Energy*, vol. 47, no. 39, pp. 17494–17503, May 2022, doi: 10.1016/j.ijhydene.2022.03.185.

[61] V. Preziosi *et al.*, “Organic electrochemical transistors as novel biosensing platforms to study the electrical response of whole blood and plasma,” *J. Mater. Chem. B*, vol. 10, no. 1, pp. 87–95, 2022, doi: 10.1039/D1TB01584B.

[62] S. Han, A. G. Polyravas, S. Wustoni, S. Inal, and G. G. Malliaras, “Integration of Organic Electrochemical Transistors with Implantable Probes,” *Adv. Mater. Technol.*, vol. 6, no. 12, p. 2100763, Dec. 2021, doi: 10.1002/admt.202100763.

[63] B. Zhu *et al.*, "Patterning Vertically Grown Gold Nanowire Electrodes for Intrinsically Stretchable Organic Transistors," *Adv. Electron. Mater.*, vol. 5, no. 1, p. 1800509, Jan. 2019, doi: 10.1002/aelm.201800509.
[64] T. Makita *et al.*, "Damage-free Metal Electrode Transfer to Monolayer Organic Single Crystalline Thin Films," *Sci. Rep.*, vol. 10, no. 1, p. 4702, Dec. 2020, doi: 10.1038/s41598-020-61536-8.
[65] Q. Li *et al.*, "Review of Printed Electrodes for Flexible Devices," *Front. Mater.*, vol. 5, p. 77, Jan. 2019, doi: 10.3389/fmats.2018.00077.
[66] X. Huang, Z. Zeng, Z. Fan, J. Liu, and H. Zhang, "Graphene-Based Electrodes," *Adv. Mater.*, vol. 24, no. 45, pp. 5979–6004, Nov. 2012, doi: 10.1002/adma.201201587.
[67] T. N. Mangoma, S. Yamamoto, G. G. Malliaras, and R. Daly, "Hybrid 3D/Inkjet-Printed Organic Neuromorphic Transistors," *Adv. Mater. Technol.*, vol. 7, no. 2, p. 2000798, Feb. 2022, doi: 10.1002/admt.202000798.
[68] H. Han, C.-H. Kim, and S. Jung, "Vertical integration: a key concept for future flexible and printed electronics," *Flex. Print. Electron.*, vol. 7, no. 2, p. 023003, Jun. 2022, doi: 10.1088/2058-8585/ac7929.
[69] J. Perelaer *et al.*, "Printed electronics: the challenges involved in printing devices, interconnects, and contacts based on inorganic materials," *J. Mater. Chem.*, vol. 20, no. 39, p. 8446, 2010, doi: 10.1039/c0jm00264j.
[70] F. Torrisi *et al.*, "Inkjet-Printed Graphene Electronics," *ACS Nano*, vol. 6, no. 4, pp. 2992–3006, Apr. 2012, doi: 10.1021/nn2044609.
[71] V. Beedasy and P. J. Smith, "Printed Electronics as Prepared by Inkjet Printing," *Materials*, vol. 13, no. 3, p. 704, Feb. 2020, doi: 10.3390/ma13030704.
[72] P. Chattoraj, K. Debnath, and A. Manmadhachary, "A Review paper on 3D-Printing Aspects and Various Processes Used in the 3D-Printing," *Int. J. Mech. Eng.*, p. 11, 2022.
[73] K. Kim, J. Park, J. Suh, M. Kim, Y. Jeong, and I. Park, "3D printing of multiaxial force sensors using carbon nanotube (CNT)/thermoplastic polyurethane (TPU) filaments," *Sens. Actuators Phys.*, vol. 263, pp. 493–500, Aug. 2017, doi: 10.1016/j.sna.2017.07.020.
[74] M. Tavakkoli Gilavan, M. S. Rahman, A. Minhas-Khan, S. Nambi, and G. Grau, "One-Step Fabrication of Low-Resistance Conductors on 3D-Printed Structures by Laser-Induced Graphene," *ACS Appl. Electron. Mater.*, vol. 3, no. 9, pp. 3867–3875, Sep. 2021, doi: 10.1021/acsaelm.1c00480.
[75] L. Jiao *et al.*, "Laser-Induced Graphene on Additive Manufacturing Parts," *Nanomaterials*, vol. 9, no. 1, p. 90, Jan. 2019, doi: 10.3390/nano9010090.
[76] Q. Li, T. Wu, W. Zhao, J. Ji, and G. Wang, "Laser-Induced Corrugated Graphene Films for Integrated Multimodal Sensors," *ACS Appl. Mater.*

Interfaces, vol. 13, no. 31, pp. 37433–37444, Aug. 2021, doi: 10.1021/acsami.1c12686.
[77] S. P. Singh, Y. Li, J. Zhang, J. M. Tour, and C. J. Arnusch, "Sulfur-Doped Laser-Induced Porous Graphene Derived from Polysulfone-Class Polymers and Membranes," *ACS Nano*, vol. 12, no. 1, pp. 289–297, Jan. 2018, doi: 10.1021/acsnano.7b06263.
[78] F. Parodi, "EniChem SpA, Milano, Italy," p. 31.
[79] B. Yao, J. Zhang, T. Kou, Y. Song, T. Liu, and Y. Li, "Paper-Based Electrodes for Flexible Energy Storage Devices," *Adv. Sci.*, vol. 4, no. 7, p. 1700107, Jul. 2017, doi: 10.1002/advs.201700107.
[80] S. Huang, Y. Liu, Y. Zhao, Z. Ren, and C. F. Guo, "Flexible Electronics: Stretchable Electrodes and Their Future," *Adv. Funct. Mater.*, vol. 29, no. 6, p. 1805924, Feb. 2019, doi: 10.1002/adfm.201805924.
[81] C. Xu, B. Xu, Y. Gu, Z. Xiong, J. Sun, and X. S. Zhao, "Graphene-based electrodes for electrochemical energy storage," *Energy Environ. Sci.*, vol. 6, no. 5, p. 1388, 2013, doi: 10.1039/c3ee23870a.
[82] D. H. Youn, J.-W. Jang, J. Y. Kim, J. S. Jang, S. H. Choi, and J. S. Lee, "Fabrication of graphene-based electrode in less than a minute through hybrid microwave annealing," *Sci. Rep.*, vol. 4, no. 1, p. 5492, May 2015, doi: 10.1038/srep05492.
[83] F. M. Smits, "Measurement of Sheet Resistivities with the Four-Point Probe," *Bell Syst. Tech. J.*, vol. 37, no. 3, pp. 711–718, May 1958, doi: https://doi.org/10.1002/j.1538-7305.1958.tb03883.x.
[84] M. Reveil, V. C. Sorg, E. R. Cheng, T. Ezzyat, P. Clancy, and M. O. Thompson, "measurement," *Rev. Sci. Instrum.*, vol. 88, no. 9, p. 094704, Sep. 2017, doi: 10.1063/1.5001830.
[85] S. Battistoni *et al.*, "Synaptic response in organic electrochemical transistor gated by a graphene electrode," *Flex. Print. Electron.*, vol. 4, no. 4, p. 044002, Nov. 2019, doi: 10.1088/2058-8585/ab4dce.
[86] S. Demuru *et al.*, "All-Inkjet-Printed Graphene-Gated Organic Electrochemical Transistors on Polymeric Foil as Highly Sensitive Enzymatic Biosensors," *ACS Appl. Nano Mater.*, vol. 5, no. 1, pp. 1664–1673, Jan. 2022, doi: 10.1021/acsanm.1c04434.
[87] "High transconductance organic electrochemical transistors," *Nat. Commun.*, vol. 4, no. 1, p. 2133, Oct. 2013, doi: 10.1038/ncomms3133.
[88] A. F. Paterson *et al.*, "On the Role of Contact Resistance and Electrode Modification in Organic Electrochemical Transistors," *Adv. Mater.*, vol. 31, no. 37, p. 1902291, Sep. 2019, doi: 10.1002/adma.201902291.
[89] S. Y. Yeung, A. Veronica, Y. Li, and I. Hsing, "High-Performance Internal Ion-Gated Organic Electrochemical Transistors for High-Frequency

Bioimpedance Analysis," *Adv. Mater. Technol.*, p. 2201116, Nov. 2022, doi: 10.1002/admt.202201116.
[90] W. Ji *et al.*, "Carbonized silk fabric-based flexible organic electrochemical transistors for highly sensitive and selective dopamine detection," *Sens. Actuators B Chem.*, vol. 304, p. 127414, Feb. 2020, doi: 10.1016/j.snb.2019.127414.
[91] J. M *et al.*, "Highly sensitive organic electrochemical transistor for detection of stress-induced cation leakage from plant cells," *Biosens. Bioelectron. X*, vol. 12, p. 100251, Dec. 2022, doi: 10.1016/j.biosx.2022.100251.
[92] D20 Committee, "Test Method for Tensile Properties of Plastics," ASTM International. doi: 10.1520/D0638-14.